INVESTIGATION OF LOW-PROFILE VORTEX GENERATORS VIA EXPERIMENTAL METHODS

By

REAL KC

Bachelor of Science in Aerospace Engineering

Oklahoma State University

Stillwater, Oklahoma

2017

Submitted to the Faculty of the
Graduate College of
Oklahoma State University
in partial fulfillment of
the requirements for
the Degree of
MASTER OF SCIENCE
July, 2019

INVESTIGATION OF LOW-PROFILE VORTEX GENERATORS

VIA EXPERIMENTAL METHODS

Thesis Approved:

Dr. Brian Elbing

Thesis Advisor

Dr. Jamey Jacob

Dr. Aaron Alexander

ACKNOWLEDGMENTS

This work was in part funded by Edge Aerodynamix. I would like to thank my parents for their unconditional love and support throughout the years. To my closest friends in the past two years: Nick and Trevor, I just want to thank you two from the bottom of my heart. I would not be where I am today without you two. I would like to thank my other friends and lab mates Zeeshan, Chris, Jacob, Mason, Shahrouz, Yasaman, Thomas, et al., for their support during my research. To my committee, thank you for your support and guidance through this journey.

Acknowledgements reflect the views of the author and are not endorsed by committee members or Oklahoma State University.

Name: Real KC

Date of Degree: July, 2019

Title of Study: INVESTIGATION OF LOW-PROFILE VORTEX GENERATORS VIA EXPERIMENTAL METHODS

Major Field: Mechanical and Aerospace Engineering

Abstract:

A novel low-profile vortex generator has recently demonstrated fuel savings of 1% on commercial aircraft. It has been termed a Conformal Vortex Generator (CVG) and consists of a backward facing step where the chord position of the step periodically varies in the spanwise direction. The fluid mechanism response for the observed fuel savings remains unclear. The current work aims to understand the behavior at subsonic conditions via two sets of experiments. The first experiment used particle-image-velocimetry in a water tunnel to study the flow over a CVG on a flat plate. Measurements were acquired immediately downstream of the peak, valley, and mid-locations as downstream distance based Reynolds numbers between 60,000 and 900,000. This study showed that with a laminar inlet the flow downstream of the peak transitions to turbulent flow while downstream of the valley it remains laminar, which results in significant spanwise variation in the velocity distribution. The second experiment used Pitot-static probes (single and multi-hole) to acquire wake surveys in a wind tunnel downstream of an LA203A airfoil with either a CVG, backward facing step, or a clean wing configuration. Multiple CVG configurations were studied at a chord based Reynolds number of 300,000 and the angle of attack varied from 0 to 10 degrees. The CVGs generated strong coherent structures that persisted at least five chord lengths in the airfoil wake. The general trend was that the smaller the CVG the weaker the coherent structures. At higher angles of attack, the coefficient of drag increased the further upstream the CVG was located. In general, CVG outperformed a backward facing step but not the clean wing configuration.

TABLE OF CONTENTS

Chapter Page

I. INTRODUCTION 1

1.1. Motivation 1

1.2. Goals and Objectives 2

II. LITERATURE REVIEW 3

2.1. Flow Control 3

2.2. Vortex Generators 3

2.3. Conformal Vortex Generators 4

2.3.1. Background 4

2.3.2. Wind Turbines 5

2.3.3. Previous OSU Research 6

III. THEORY 9

3.1. Governing Equations 9

3.2. Boundary Layer 9

3.2.1. Laminar Boundary Layer 9

3.2.2. Transition 11

3.2.3. Turbulent Boundary Layer 13

3.3. Flat Plate Scaling 14

3.4. Particle Image Velocimetry 17

3.5. Lift and Drag 18

IV. EXPERIMENT I: BOUNDARY LAYER INVESTIGATION 20
4.1. Experimental Methods 20
4.1.1. Facility 20
4.1.2. Test Model 20
4.1.3. Instrumentation 21
4.1.4. Test Matrix 22
4.2. Results 23
4.3. Discussion 26
4.3.1. Uncertainty Analysis 27
4.4. Conclusions 30

V. EXPERIMENT II: WAKE SURVEY 31
5.1. Experimental Methods 31
5.1.1. Facility 31
5.1.2. Test Model 31
5.1.3. CVG Configurations 33
5.1.4. Instrumentation 34
5.1.5. Experimental Method 36
5.1.6. Test Matrix 38
5.2. Results 38
5.3. Discussion 39
5.3.1. Clean Wing 39
5.3.2. Backward facing step 40
5.3.3. CVG 42
5.3.4. Phase II 44
5.3.5. Phase I and II comparison 54
5.3.6. Uncertainty Analysis 54
5.4. Conclusions 56

5.4.1. Phase I 57
5.4.2. Phase II 57

VI. CONCLUSIONS AND RECOMMENDATIONS 60
6.1. Boundary Layer Investigation 60
6.2. Wake Survey 61
6.2.1. Phase I 61
6.2.2. Phase II 62
6.3. Recommendations 62

REFERENCES 63

APPENDICES 67

LIST OF FIGURES

Figure		Page
1	An example of a triangle-shaped vortex generator [3].	4
2	Two diffrent configurations of CVGs applied to a helicopter blade. Top image shows the overall application while the bottom shows the two different CVG types [12].	6
3	Schematic of the CVG tape applied to the Boeing 737 aircraft. The blue outline demonstrates the location of CVGs [12].	7
4	CVG applied to the NREL Wind Turbine [14].	8
5	Falkner-Skan profiles of stream-wise velocity in a laminar boundary layer [19]	11
6	Schematic of flow over over a flat plate. The location of transition can be seen near the end of the flow, right before where turbulence occurs [19] . . .	12
7	Side and top view schematic of a CVG as a list of parameters required to characterize the geometry, inlet condition, and the CVG influence [20] . . .	15
8	A generic lift and drag coefficients for a wing [19]	19
9	Flat plate model with CVG configuration.	21
10	Picture of the water Tunnel test section with the flat plate and the PIV system.	23
11	Picture of the all the location where data was collected	24
12	Velocity profiles downstream of (a) peak and (b) valley	25
13	(a) raw Boundary layer profile, (b) BL profile with freestream velocity (c) scaled boundary layer profiles	25

14 Flat plate boundary layer profile for multiple speeds at : (a) x = 158 mm, (b) x = 370 mm. 26
15 Boundary layer velocity profiles downstream of (a) peak, (b) mid, and (c) valley. 27
16 Scaled momentum thickness vs. downstream distance based Reynolds number. For reference, lines corresponding to the momentum thickness for turbulent and laminar and flat plates are shown. 28
17 Shape factor plotted vs. downstream distance based Reynolds number. All data was acquired on a flat plate model in a water tunnel. For reference, lines corresponding to the shape factor for turbulent and laminar flat plate are shown. 28
18 (top) A picture and (bottom) schematic of the Oklahoma State University Subsonic Wind Tunnel [18] 32
19 LA203A Wing Profile. 32
20 (a) Schematic of CVG V1.0; (b) CVG V1; (c) CVG V2, and (d) CVG V3 and V4. 35
21 Schematic of the five hole probe coordinate system and variables. 36
22 Test section instrumentation and simple schematic of the wake survey system. 37
23 Side and top view of the wake survey system relative to the wing model. . . 37
24 (a) Raw wake profile from a single spanwise location, (b) raw wake profiles from multiple spanwise locations. 39
25 Velocity u for clean wing at 0 degrees angle of attack 40
26 (a) Contour plot of wake at Reynolds number of 300,000 for the clean wing; (b) C_D of the clean wing with Xfoil estimation. 41
27 (a) Contour plot of wake at Reynolds number of 300,000 for BFS at 27% chord length; (b) C_D plots of the BFS plotted against the angle of attack and compared with the clean wing. 41

28 Contour plot of the wake 5 chord lengths downstream of the model at Reynolds number of 300,000 with CVG-V1. The origin of the abscissa lined up with the mid-location between a peak and valley. 42

29 (a) Contour plot of wake at Reynolds number of 300,000 for CVG V2; (b) C_D plots of all of the CVG configurations plotted against the clean wing. . . 43

30 Contour plots of the (left column) u, (middle column) v, and (right column) w velocity components at (top row) 0°, (middle row) 4°, and (bottom row) 8° angle of attack for the clean wing. All data acquired at Re = 300,000. . . 45

31 (Left column) Magnitude plot and (right column) vorticity plot of the clean wing at (top row) 0°, (middle row) 4°, and (bottom row) 8° angle of attack. All data acquired at Re = 300,000. 46

32 Contour plots of the (left column) u, (middle column) v, and (right column) w velocity components of (top row) BFS at 10% and (bottom row) BFS at 45%. All data acquired at Re = 300,000 and 0° angle of attack. 48

33 (Left column) Magnitude plot and (right column) vorticity plot of the (top row) BFS at 10% and (bottom row) BFS at 45%. All data acquired at Re = 300,000 and 0° angle of attack. 49

34 Contour plots of the (left column) u, (middle column) v, and (right column) w velocity components at (top row) 0°, (middle row) 4°, and (bottom row) 8° angle of attack for CVG-V1. All data acquired at Re = 300,000. 51

35 (Left column) Magnitude plot and (right column) vorticity plot of CVG-V1 at (top row) 0°, (middle row) 4°, and (bottom row) 8° angle of attack. All data acquired at Re = 300,000. 52

36 Average vorticity for the wake of all the configurations 53

37 Comparison of clean wing and CVG-V1 between phase I and II 54

38 Uncertainty of C_D at across the CVG. 55

39 Comparison of clean wing and CVG-V1 between phase I and II with error bars 56
40 C_D plot comparing the best CVG, best BFS, and the clean wing results. . . . 58
41 Flow visualization of the flow downstream of CVG-V2 (top) peak, (middle) mid peak-valley, and (bottom) valley. 68

LIST OF TABLES

Table		Page
1	Nominal independent parameters from flight scale testing	15
2	Required water tunnel testing conditions based on number of film layers . .	17
3	Geometric parameters of the flat plate test article.	23
4	Test matrix of the conducted tests.	24
5	Dimensions of the different testing configurations.	34
6	Test matrix of the conducted tests	38

NOMENCLATURE

α	=	angle of attack
δ	=	boundary layer thickness
δ^*	=	boundary displacement thickness
δ_{99}	=	boundary layer thickness at 99% U_∞
ϵ	=	uncertainty
μ	=	dynamic viscosity
ν	=	kinematic viscosity
ω	=	vorticity
ρ	=	air density
σ	=	standard deviation
θ	=	boundary momentum thickness
b	=	wing span
c	=	chord
CVG	=	Conformal Vortex Generator
C_D	=	coefficient of drag
C_L	=	coefficient of lift
D	=	drag
g	=	gravitational force
H	=	CVG height or shape factor
K	=	relaminarization parameter
p	=	pressure
Re	=	Reynolds number

Re_c = Reynolds number based on chord length

Re_H = Reynolds number based on CVG height

Re_x = Reynolds number based on downstream distance

t = time

u = streamwise Velocity (x-direction)

U = streamwise Velocity (x-direction)

U_∞ = free-stream velocity

v = vertical velocity (y-direction)

w = Spanwise velocity (z-direction)

W = CVG width

x = Spanwise distance of the wing

y = vertical distance from the maximum wake deficit

$y_{1/2}$ = half deficit of the wake

z = spanwise distance of the wing

CHAPTER I

INTRODUCTION

1.1. Motivation

Aerodynamic performance enhancement is a major priority for the airline industry. An essential mean of improving the aerodynamic performance of an aircraft is through drag reduction. Drag reduction reduces the fuel consumption of aircraft, lowering the cost of fuel for all the airlines. Lower fuel consumption leads to a reduction in the carbon emission from aircraft, making air travel more environmental friendly. Drag reduction can be achieved through two types of flow control: passive or active method. Active methods achieve higher drag reduction, but are often offset by the energy consumption, added maintenance, and design complexity. Therefore, the most common drag reduction methods that have been successful are passive. An example of a passive flow control device are vortex generators (VG). VGs are commonly used in aircraft to re-energize the wing's boundary layer to delay flow separation and aerodynamic stalling[1, 2]. Conventional VGs consist of a small vane that is orthogonal to the surface and on the same order of magnitude of boundary layer thickness. The current work characterizes a low-profile vortex generator that was termed Conformal Vortex Generator (CVG). There has been evidence of fuel savings of over 1% on a Boeing 737, but the mechanism behind the savings are still unclear. More background information on CVGs is provided in section 2.3.1. The current work focuses on two areas:

Boundary layer investigation of the flow over a CVG with laminar inlet and wake survey of CVGs on a wing model.

1.2. Goals and Objectives

The goal of this study was to investigate the flow field induced by the CVGs via detailed experiments on a flat plate and an airfoil model. The primary objective was to identify the dominant fluid mechanism responsible for drag reduction observed on commercial aircraft equipped with CVGs. For the flat plate water tunnel study, the following tasks were carried out:

- Validate the clean flat plate boundary layer with literature. Compare the results with the Blasius boundary layer solution.
- Qualitatively and quantitatively compare the velocity profiles at different locations downstream of the CVG.
- Study the effects of CVG through boundary layer characteristics.

For the airfoil in a wind tunnel study, the following tasks were carried out:

- Compare the clean wing data with literature.
- Study the effects of a backwards facing step at different locations on a wing and compare the drag coefficients with clean wing and literature.
- Study the wake of multiple CVG configurations and compare the drag coefficients with the clean wing and the backwards facing steps.

CHAPTER II

LITERATURE REVIEW

2.1. Flow Control

One of the essential means of enhancing the aerodynamic performance on an aircraft is through flow control [1, 3]. There are two main types of flow control, active and passive flow control. Passive flow control, in theory, requires no additional energy, while active flow control devices require energy and must be driven in a time dependent manner [4]. These devices may be turned on and off during a flight, depending the flight regime to achieve ideal control. Examples of active flow control devices include valves and plasma actuators. The most common example of passive flow control is the use of vortex generators.

2.2. Vortex Generators

A common passive flow control device is a vortex generator (VG). VGs are commonly used on aircraft to control the wing aerodynamic boundary layer. It does so by re-energizing the boundary layer to delay flow separation and aerodynamic stalling [1, 2]. For small ultralight aircraft, VGs can significantly reduce the stall speed and provide better stall progression in terms of aileron maneuverability [5]. Whereas, for aircraft that operate in the transonic and supersonic regime, VGs can also alleviate shock interaction with the boundary layer [6]. Although VGs are commonly known for their applications in aircrafts,

they are also applicable in the automotive industry. Dubey et al. [7] showed that the application of VGs reduced drag for hatchback and sedan models that were tested.

Many VG variants can be found throughout the aircraft industry and literature. Fig. 1 shows an example of the common triangle shaped vortex generators seen in most applications [3]. Studies on vortex generation flow control devices have primarily been focused on adding momentum to the boundary layer or using trips to initiate transition with leading edge devices. In general, manipulation of the boundary layer has been the main objective for flow control, either for separation control or drag reduction. In order to achieve this, certain devices such as vortex generator jets (VGJs) or zero-net mass flux synthetic jets and plasma actuators in various configurations have been used. Active, as opposed to passive, vortex generators have been an active area of research [8, 9]. However, these systems require direct energy input. Active vortex generators that are conformal in nature are also possible, such as plasma vortex generators (PVG), but since they are active, these also require energy input [10, 11].

Figure 1: An example of a triangle-shaped vortex generator [3].

2.3. Conformal Vortex Generators

2.3.1. Background

Fig. 2 shows the type of vortex generator that is the focus of this study, which have been termed a Conformal Vortex Generator (CVG). CVG is a thin layer of tape with triangle shaped serrated edges that is applied near the leading edge of a wing, typically downstream of

the slat step. CVGs were originally developed by Edge Aerodynamix to mitigate efficiency losses associated with applying protective leading edge tape to helicopter rotor blades [12]. Protective tapes or coatings have been studied previously and were shown to protect the helicopter rotors blades while significantly increasing the profile drag [13]. The application of CVGs, however, not only protected the rotor blades, but also increased the fuel efficiency of the helicopter. Field tests were conducted with the same CVG configurations applied to different aircraft, including a Boeing 737-500. A schematic of the CVG application on this aircraft is shown in Fig. 3 The CVG was placed at 10 percent chord length of the wing, right behind the slat step. The thickness of this tape was 0.367 mm. Fuel savings of up to 6 percent was seen with the CVGs being applied. Although the conclusion was that the CVGs could increase fuel efficiency, little was known about the actual physical mechanism responsible for the improvements.

2.3.2. Wind Turbines

A study was done using wind turbines by the National Renewable Energy Laboratory (NREL) [14]. Typically, a tape is applied to the leading edge of wind turbine blades for two purposes; improve the power capture of the turbine and/or extend the turbine lifetime, or both. The NREL project tested the performance of a commercially available leading edge tape and compared it to the performance of CVGs. Fig. 4 shows NREL's wind turbines with CVGs applied to them.The turbines were 2-bladed Westinghouse WWG-0600 turbines with the rotor diameter of approximately 44 m. The power output of the turbine for the two configurations was recorded and compared against each other. The results showed KWH production increased by 6% for the CVGs at 7 m/s wind speed and grew to 7.4% at 11 m/s and above wind speed. The study only looked at turbine efficiency; therefore, no information about thefluid mechanism responsible for the improved performance was produced.

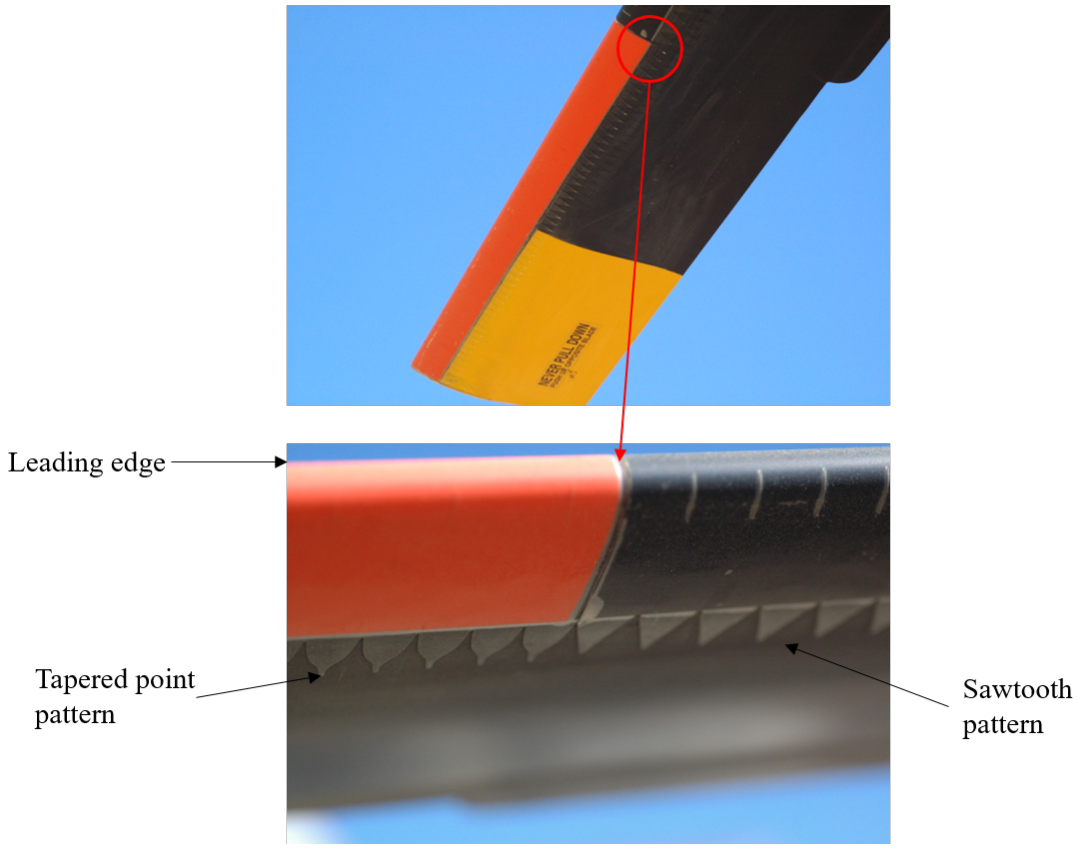

Figure 2: Two diffrent configurations of CVGs applied to a helicopter blade. Top image shows the overall application while the bottom shows the two different CVG types [12].

2.3.3. Previous OSU Research

Understanding the physics behind the CVGs, evaluating their effect on the flow field, and characterizing the drag reduction mechanism were Kibble's [15] objectives. Kibble [15] used experimental and computational tools to conduct his research. Star-CCM+, a commercially available CFD software, was used for all of the computational research. The CVG configurations in Star-CCM+ were created to match that of the flight conditions. Kibble [15] was able to show that the wall shear stress patterns from simulations were very similar to the data captured from actual flight tests. Kibble [15] concluded that a potential source for drag reduction was from shock stabilization; however, further investigation was still required.

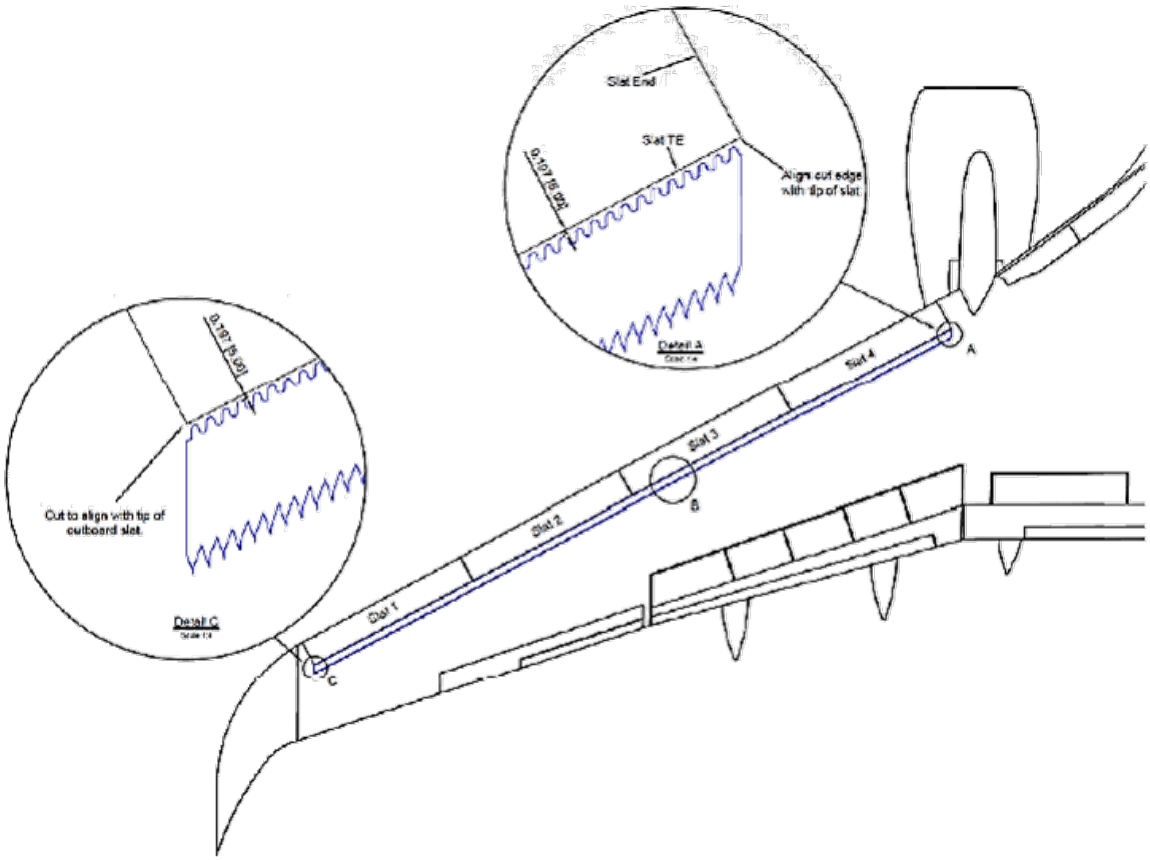

Figure 3: Schematic of the CVG tape applied to the Boeing 737 aircraft. The blue outline demonstrates the location of CVGs [12].

Lucido et al. [16] conducted a water tunnel experiment to study the evolution of a boundary layer downstream of the CVG with a laminar inlet. The results were compared to results from a Piper Cherokee and both showed a clear spanwise variation in the velocity distribution. The water tunnel experiment also showed that the flow downstream of the peak transitions to a turbulent flow earlier than the upstream valley. Using boundary layer properties, the experimental results were compared with computational results in Wilson et al. [17]. The results showed that the shape factor of the boundary layer matched extremely well between the computational and experimental work. Wilson et al. [17] also modeled the flight condition CVGs applied to Boeing 737 and was able to show that CVGs can generate strong coherent structures that persist downstream. KC et al.[18] studied the wake of a wing with multiple CVG configurations in a wind tunnel. KC et al.[18] was also able to show that

Figure 4: CVG applied to the NREL Wind Turbine [14].

the CVGs can produce strong coherent structures that persist downstream in the far wake region.

CHAPTER III

THEORY

3.1. Governing Equations

The governing equations for the current study are shown in equations 1 and 2. The continuity equation is given as:

$$\frac{1}{\rho}\frac{D}{Dt}\rho + \nabla \cdot \vec{u} = 0. \tag{1}$$

The Navier-Stokes equations is given as:

$$\rho\frac{Du_j}{Dt} = -\frac{\partial p}{\partial x_j} + \rho g_j + \mu\frac{\partial^2 u_j}{\partial {x_i}^2} + (\mu_v + \frac{1}{3}\mu)\frac{\partial}{\partial x_j}\frac{\partial u_m}{\partial x_m}. \tag{2}$$

These equations were directly used or a different form of the equations were used in the two experiments conducted.

3.2. Boundary Layer

3.2.1. Laminar Boundary Layer

Boundary layer theory is a well defined and well established theory, especially for laminar boundary layers. For a zero-pressure gradient flat plate, a laminar boundary layer has an exact solution, the Blasius solution [19]. The results of the Blasius solution are provided in equations 3, 4, and 5. The momentum thickness, θ, is the momentum loss in the actual

flow because of the presence of the boundary layer whereas, the displacement thickness, δ^*, is the distance the wall would have to be displaced outward in a hypothetical friction-less flow to maintain the same mass flux as the actual flow [19]. From the momentum and displacement thickness relationships, the shape factor can also be calculated, as shown in Equation 6. The shape factor is used to determine the nature of the flow.

The δ_{99} equation is given as:

$$\delta_{99} = \frac{4.92x}{{Re_x}^{1/2}}. \tag{3}$$

The displacement thickness is given as:

$$\delta^* = 1.72\sqrt{\frac{\nu x}{U}}. \tag{4}$$

The momentum thickness is given as:

$$\theta = 0.644\sqrt{\frac{\nu x}{U}}. \tag{5}$$

the shape factor is given as:

$$H = \frac{\delta^*}{\theta} = 2.67. \tag{6}$$

In the case of a flat plate with a pressure gradient, the Falkner-Skan similarity solutions can be used instead of the Blasius solution. The Falkner-Skan similarity equation is given as:

$$f''' + \frac{n+1}{2} f f'' - n f'^2 + n = 0. \tag{7}$$

and the similarity variable (η) is given as:

$$\eta = y\sqrt{\frac{a}{\nu}} x^{(n-1)/2}. \tag{8}$$

The f in the Falkner-Skan equation is an unknown dimensionless function [19]. Given the boundary conditions, the Falkner-Skan equation can be computed using numerical

methods. Fig. 5 shows the numerical solution for various values of n.

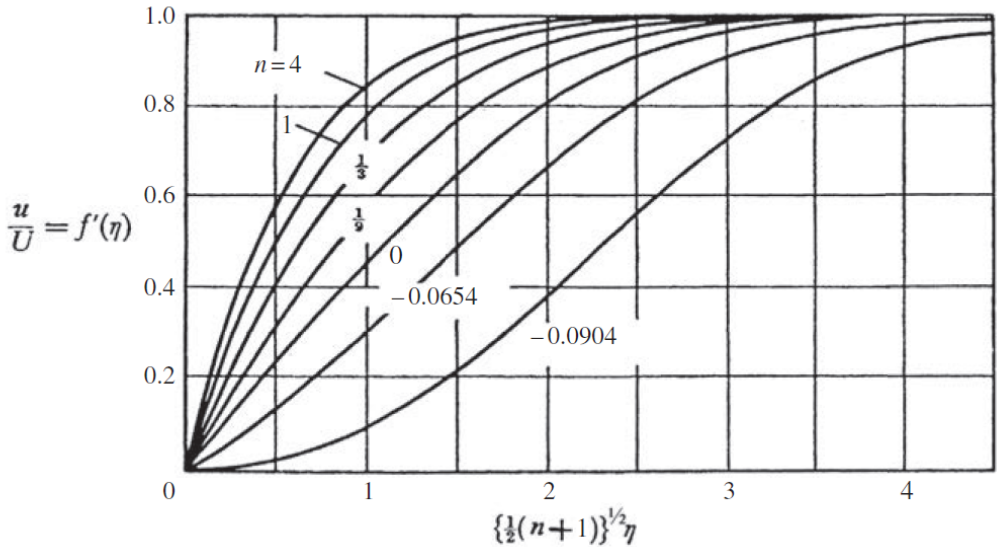

Figure 5: Falkner-Skan profiles of stream-wise velocity in a laminar boundary layer [19]

3.2.2. Transition

When the boundary layer transitions from laminar to turbulent, the solutions presented in the laminar section become invalid. There are multiple ways a flow transitions, whether it be because of the laminar boundary layer being unstable or because of a forced mechanism. The location of transition from laminar to turbulent is important for many flow applications. For example, for an airfoil, it is better to have a flow transition further downstream, as the drag can be reduced because of it. A schematic of a flow over a flat plate is shown in Fig. 6, which includes transition [19]. In an experimental study, a flow can be forced to transition to turbulence with the addition of a trip wire or sand-grain roughness (eg. sandpaper).

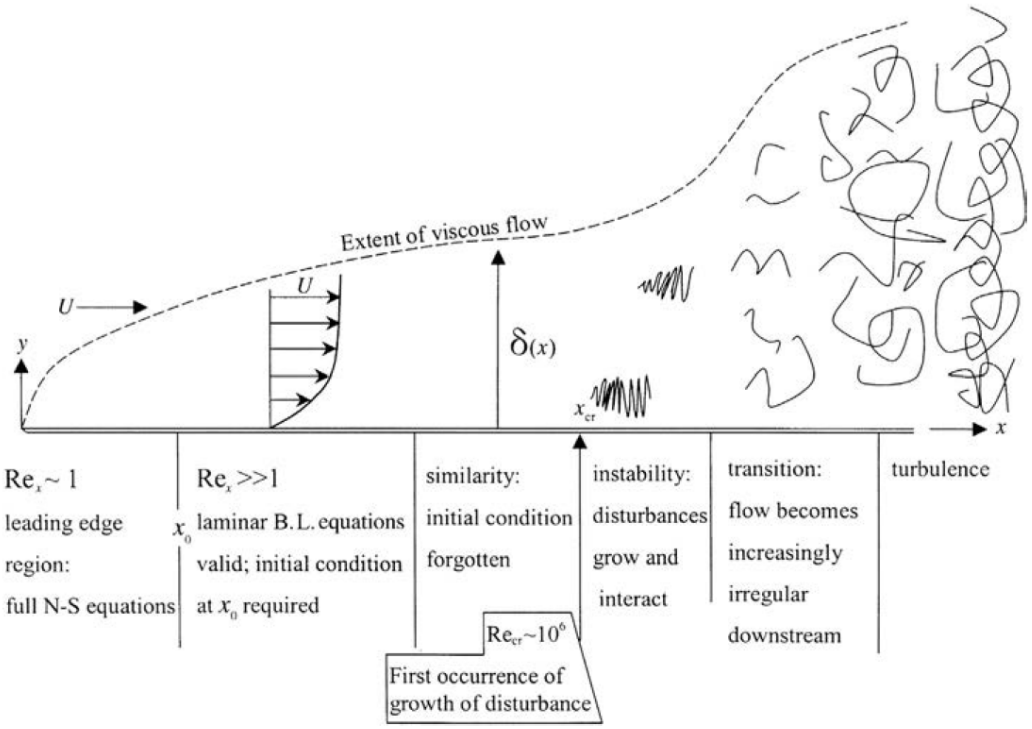

Figure 6: Schematic of flow over over a flat plate. The location of transition can be seen near the end of the flow, right before where turbulence occurs [19]

3.2.3. Turbulent Boundary Layer

A flow transitions from laminar to turbulent if there is some kind of disturbance in the flow or the Reynolds number of the flow is sufficiently high. Generally, in terms of air flow over a wing, turbulent flows are less desirable than laminar ones. The turbulent boundary layer is thicker and is associated with high wall shear stress, thus high skin friction drag. The displacement and the momentum thickness can be found by using their actual definitions, instead of the approximation discussed in the laminar section. However, a turbulent boundary layer can also be approximated.

The actual displacement thickness equation is given as:

$$\delta^* = \int_0^\infty (1 - \frac{U}{U_\infty})dy. \tag{9}$$

The actual momentum thickness is given as:

$$\theta = \int_0^\infty \frac{U}{U_\infty}(1 - \frac{U}{U_\infty})dy. \tag{10}$$

The approximated displacement thickness of a turbulent boundary layer is given as:

$$\frac{\delta^*}{x} \cong \frac{0.020}{Re_x^{1/7}}. \tag{11}$$

The approximated momentum thickness of a turbulent boundary layer is given as:

$$\frac{\theta}{x} \cong \frac{0.016}{Re_x^{1/7}}. \tag{12}$$

For the CVG Boundary layer study, the actual equation was used to the estimate the displacement thickness, momentum thickness, and the shape factor from the collected data. The experimental values were then compared against the approximated solutions.

3.3. Flat Plate Scaling

The current work focuses solely on flow over a CVG with a laminar boundary layer inlet, and it is assumed the parameter of interest is the vorticity field downstream of the CVG (ω). While this statement assumes a drag reduction mechanism, the same analysis would be valid for any other downstream parameter being considered (e.g. pressure distribution, shear stress, etc). The current working model (illustrated in Fig. 7) assumes that the impact of the CVG can be assessed based on the inlet boundary layer condition, CVG geometry (height, H; width, W; and length L), and the fluid properties (density, ρ; and kinematic viscosity, ν). While the boundary layer properties are dependent on the upstream history, locally at the CVG with a laminar boundary layer inlet (i.e. fixed shape) it can be fully characterized based on the thickness (δ), the freestream velocity (U_∞), and the pressure gradient ($\frac{\mathrm{d}p}{\mathrm{d}x}$). If the working model is valid, dimensional reasoning states that there exists a function ϕ such that

$$\frac{\omega H}{U_\infty} = \phi\left(\frac{\delta}{H}, \frac{U_\infty H}{\nu}, \frac{\mathrm{d}p}{\mathrm{d}x}\frac{H}{\rho U_\infty^2}, \frac{W}{H}, \frac{L}{H}\right). \tag{13}$$

This analysis is also included in [16] and [20].

This scaling law states that if the five (independent) parameters on the right hand side are matched between two tests, the resulting flow downstream of the CVG must also be matched. Thus the objective of the current experiments is to match the five independent parameters between the flight scale and laboratory testing. The flight scale shear stress measurements serve as a validation for both the working model as well as any assumptions required to match parameters between flight and laboratory testing.

The most difficult flight condition to identify is the inlet boundary layer condition at the CVG location. As an upper bound, the Blasius laminar boundary layer solution for a flat plate ($\mathrm{d}p/\mathrm{d}x = 0$) sets $\delta \approx 1\,\mathrm{mm}$. This was further refined using Xfoil[21] to be $\delta \approx 0.693\,\mathrm{mm}$ with $\mathrm{d}p/\mathrm{d}x \approx -412\,\mathrm{Pa/m}$. While several CVG geometries were tested, the initial sizing used here is based on the CVG currently implemented on the Boeing 737

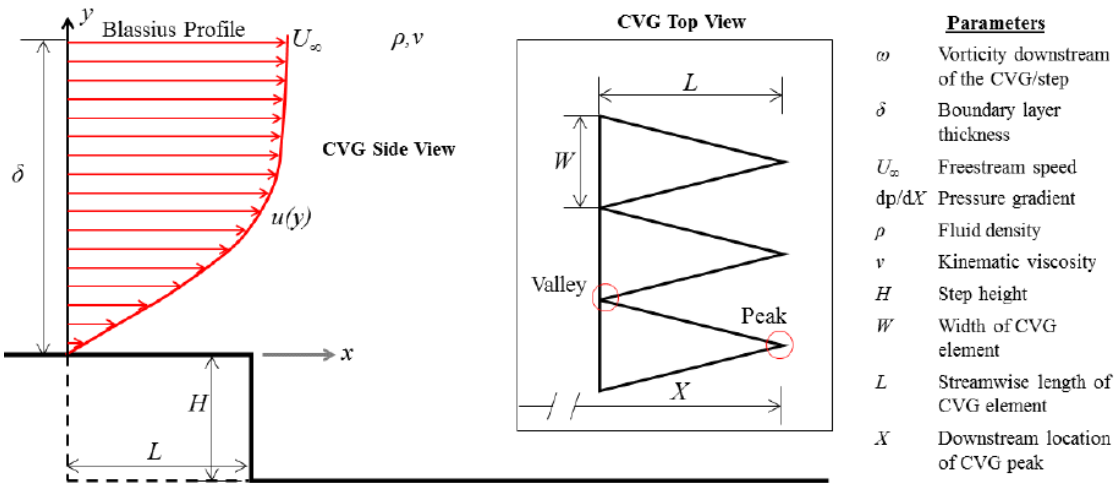

Figure 7: Side and top view schematic of a CVG as a list of parameters required to characterize the geometry, inlet condition, and the CVG influence [20]

($H = 0.367$ mm, $W = 17.1$ mm, $L = 23.5$ mm). These values combined with atmospheric properties at $\sim$ 1000 m above sea level are used to calculate the independent parameters, which are summarized in Table 1.

Table 1: Nominal independent parameters from flight scale testing

Parameter	Flight Scale Value
δ/H	1.89
Re_H	1700
$\frac{dp}{dx}\frac{H}{\rho U_\infty^2}$	$-2.7 \times 10^{-}5$
W/H	47
L/H	64
K	1.6×10^{-8}

A more traditional method for quantifying the pressure gradient is using the K parameter [22],

$$K = \frac{\nu}{U_\infty^2}\frac{dU_\infty}{dx}. \tag{14}$$

Noting that $\mathrm{d}p/\mathrm{d}x = -\rho U_\infty \, \mathrm{d}U_\infty/\mathrm{d}x$, the K parameter can be rearranged in terms of the product of two of the independent parameters in Eq. 13,

$$K = -\frac{\nu}{\rho U_\infty^3}\frac{\mathrm{d}p}{\mathrm{d}x} = -\left(\frac{\mathrm{d}p}{\mathrm{d}x}\frac{H}{\rho U_\infty^2}\right)\left(\frac{1}{Re_H}\right), \tag{15}$$

where $Re_H = U_\infty H/\nu$. Patel [23] showed that when $K < 1.6 \times 10^{-6}$, the log-region has negligible variation. This suggests that when this criteria is satisfied, the pressure gradient has a negligible impact on the resulting flow-field.

The film thickness of the CVGs, as supplied from the manufacturer, was not varied. Thus for manufacturing purposes, only heights that can be layered discretely such that the height can be expressed as $H = nH_{\text{film}} = n(0.367\,\text{mm})$, where n is a natural number, were considered for the laboratory testing. This significantly constrains the design space for the scale model testing. Rearranging the definition of Re_H, the required water tunnel test speed as a function of n is established in terms of the flight scale Re_H,

$$U_\infty = \frac{(Re_H)_{fs}\nu}{H} \approx \frac{4.67}{n} \text{ for water.} \tag{16}$$

Similarly, model boundary layer thickness can be expressed in terms of the flight scale conditions and n,

$$\delta_m = nH_{\text{film}}\left(\frac{\delta}{H}\right)_{fs} \approx n(0.7\,\text{mm}). \tag{17}$$

For a laminar, zero pressure gradient (ZPG) flat plate the Blasius boundary layer solution[19] gives

$$\frac{\delta}{x} = \frac{4.92}{\sqrt{Re_x}}. \tag{18}$$

Eq. 18 can be rearranged given that $(\delta/H) = (\delta/x)(x/H)$ such that

$$x_m = \left(\frac{\delta}{H}\right)_{fs}^2\left(\frac{nH}{4.92}\right)^2\left(\frac{U_\infty}{\nu}\right)_m. \tag{19}$$

Using Eqs. 16, 17, and 19; operation conditions for scaled testing in the water tunnel for a given film thickness n can be determined. Several thicknesses are tabulated for comparison in Table 2.

Table 2: Required water tunnel testing conditions based on number of film layers

n	U_∞ (m/s)	δ (mm)	x (mm)
1	4.7	0.7	93
2	2.3	1.4	186
3	1.6	2.1	279
4	1.2	2.8	371
5	0.94	3.5	464
6	0.78	4.2	557

3.4. Particle Image Velocimetry

Particle image velocimetry (PIV) is one of the most common experimental methods to study a given flow, whether it be in water or air. PIV captures the flow field of illuminated particles in the test section. It is important that the particles in the flow not only follow all flow velocity fluctuations but are also in sufficient number to provide the desired spatial or temporal resolution of the flow velocity. The most commonly used particles for PIV in water are latex, sphericell and in this case, hollow glass spheres. The hollow sphere is illuminated by high-intensity laser that can produce two powerful pulses to capture two images within a very short period of time. Since the laser pulses have a very short duration, it is important to precisely time the pulses of the laser with the triggering of the camera. For 2D PIV, the laser beam must be focused and spread to produce a thin sheet that will become the vector plane. The camera must be rigidly placed to avoid any movement and be aligned and focused with the laser sheet to properly capture the illuminated particles. After the image pairs are captured, they are processed within small interrogation windows. The processing software identifies the same cluster particle in both of the images and calculates the distance travelled by the particle. Since the time frame between the two images are known, the pixel movement per unit of time can be calculated. The camera must be spatially

calibrated prior to taking data for correct velocity vector field output. The calibration allows the software to identify the distance per camera pixel. Using this information, the velocity of a particle is calculated and thus, the velocity field [24].

3.5. Lift and Drag

The aerodynamic force on a moving body can be resolved into drag force, D, that is parallel to the oncoming stream, and a lift force, L, that is normal to the oncoming stream [19]. The primary means of quantifying performance are the coefficients of lift and drag. The coefficient of lift is given as:

$$C_L \equiv \frac{L}{(1/2)\rho U^2 A}. \tag{20}$$

The coefficient of drag is given as:

$$C_D \equiv \frac{D}{(1/2)\rho U^2 A}, \tag{21}$$

where A is a reference area. The wing study results are usually presented as C_D and C_L vs angle of attack, α, plots. An example of a typical C_D and C_L vs α plot is shown in Fig. 8 [19]. As the angle of attack increases, so does the coefficient of drag. For the wake survey study, the coefficient of drag will be used to compare between the different CVG configurations.

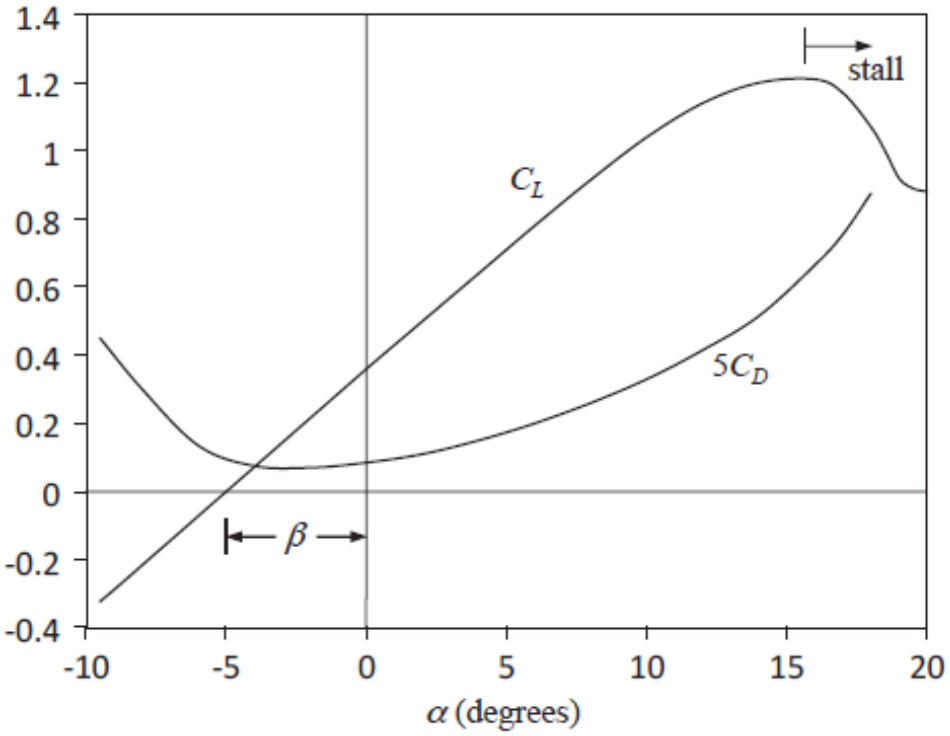

Figure 8: A generic lift and drag coefficients for a wing [19]

CHAPTER IV

EXPERIMENT I: BOUNDARY LAYER INVESTIGATION

4.1. Experimental Methods

4.1.1. Facility

The CVG boundary layer study was conducted in the 30 cm water tunnel (Model 503, Engineering Lab Design) at Oklahoma State University. The tunnel test section had an approximate length of 1 m and a 30 cm by 30 cm cross section. Due to the heavy usage of optical instruments, the test section was made from acrylic. The flow in the tunnel was powered and controlled by two independent centrifugal pumps. The maximum speed for the tunnel was 1.1 m/s with no blockage and the minimum speed was .01 m/s and. The tunnel speed was varied by changing the frequency of the pumps.

4.1.2. Test Model

Fig. 9 shows the custom built flat plate with CVGs installed. The leading edge of the flat plate was designed to be 5:1 elliptical shape to ensure a smooth flow (i.e. remain laminar) before the flat part of the plate. The plates dimensions were 750 mm long, 300 mm wide, and 12.7 mm thick. An adjustable wooden flap was added to the trailing edge to vary the pressure gradient on the plate because it can be shown that the laminar-turbulent transition would occur prior to matching other independent parameters. However, for this

experiment, the pressure gradient was set close to zero. The wooden flap was kept attached to the plate to ensure stability when the water tunnel was running. To achieve the desired thickness of the CVG, 4 layers of CVG tape (n = 4) were stacked on top of each other. Therefore, the final CVG height was approximately 1.5 mm. Accordingly, the CVG length was scaled to be L = 105 mm and the width W = 76 mm.

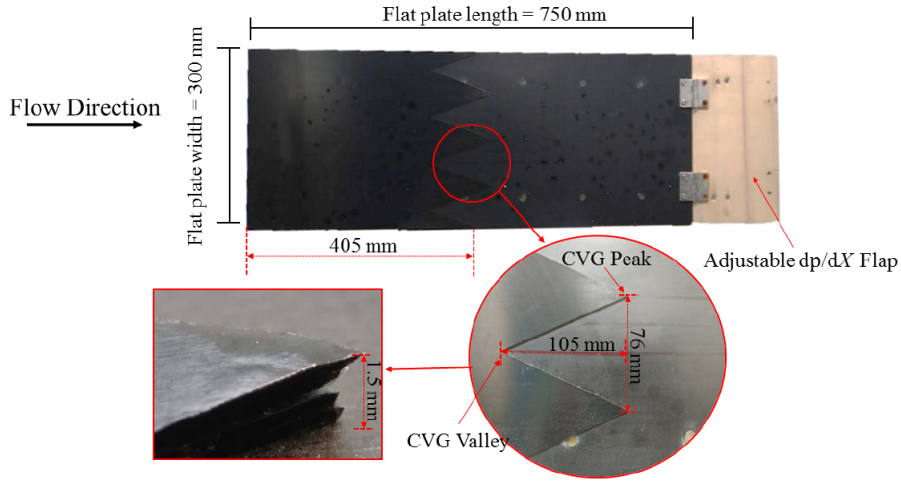

Figure 9: Flat plate model with CVG configuration.

4.1.3. Instrumentation

To investigate the boundary layer downstream of the CVGs, a two-dimensional particle image velocimetry (PIV) system was used. The PIV system laser was a Big Sky Laser Technology Nd:YAG laser. The lasers had a power output of 75 mJ/pulse at 532 nanometer wavelength. Pulse duration at this frequency was six nanoseconds. The maximum repetition rate of these lasers was 15Hz. As shown in Fig. 10, the lasers were mounted to an optics table for stability and the ability to traverse the length of the test section. The camera that was used was Redlake Motion Pro X3 camera that had a resolution of 1280x1024 pixels. The maximum frame rate attainable was 1000 frames per second. The lens that was used was the Navitar Zoom 7000 macro lens that had a focal range of 12.7 cm

to 30.5 cm. The macro lens could be taken out and a focal range of 61 cm to infinity could be obtained. Laser and camera timing was controlled by a Global Specialist Instrument's 400I Pulse generator and a Quantum Model 9518 pulse generator in tandem. The first unit controlled the overall timing, while the second unit was used as a delay generator. Image acquisition was done through Motion Studio 2.12.2, the software that was provided with the camera.

To conduct PIV, 100 image pairs were taken for each speed at all of the locations. The field-of-view for this setup was 20 mm by 30 mm. This meant that the pixels per millimeter ratio was roughly 32. After collection, the raw image files were imported to DaVis 8.2.1 for postprocessing. A new calibration function was generated by using 14 by 14 unit grid for each test. A strong, linear sharpening filter was applied to the raw calibration images and subsequently averaged. This new calibration image was used to create a third order polynomial calibration function fit. The standard deviation of the calibrated fit was kept below 3 pixels. A square mask was applied to the images so that velocity vectors were only calculated inside this region. Multi-pass processing with decreasing interrogation window size was used to compute the vector field. After starting with an initial window size of 128 by 128 pixels with 50% overlap, the final interrogation window was 16 by 16 pixels with 75% overlap. An approximate 340 by 270 vectors were calculated per vector field. Vector fields were calculated from each image pair, as well as an ensemble average. MATLAB was then used for data analysis.

4.1.4. Test Matrix

To investigate the boundary layer downstream of the CVG, 4 different freestream velocities (0.1 m/s, 0.6 m/s, 0.9 m/s, and 1.2 m/s) were tested. Table 3 shows the flow scaling parameters based on the freestream velocity. A total of 34 datasets were taken downstream of the CVGs. Fourteen sets were collected downstream of peak and valley while the last six were collected downstream of the midpoint between peak and valley. Fig. 11 shows the

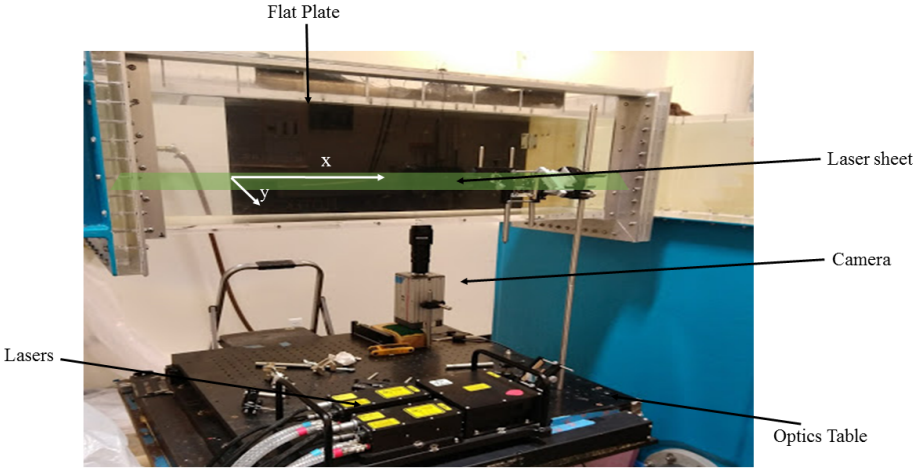

Figure 10: Picture of the water Tunnel test section with the flat plate and the PIV system.

diagram of all of the locations where data were collected. After data were collected at each location, the optical table was traversed 20 mm downstream to capture the next location. Table 4 shows the test matrix of the collected dataset.

Table 3: Geometric parameters of the flat plate test article.

Parameter	Flat Plate Value
H	1.5 mm
L	105 mm
W	76 mm
X	300 mm
L/H	70
W/H	51

4.2. Results

Using MATLAB, the velocity profiles of each data set were extracted and plotted. Shown in Fig. 12 are the velocity profiles directly downstream of the peak and the valley

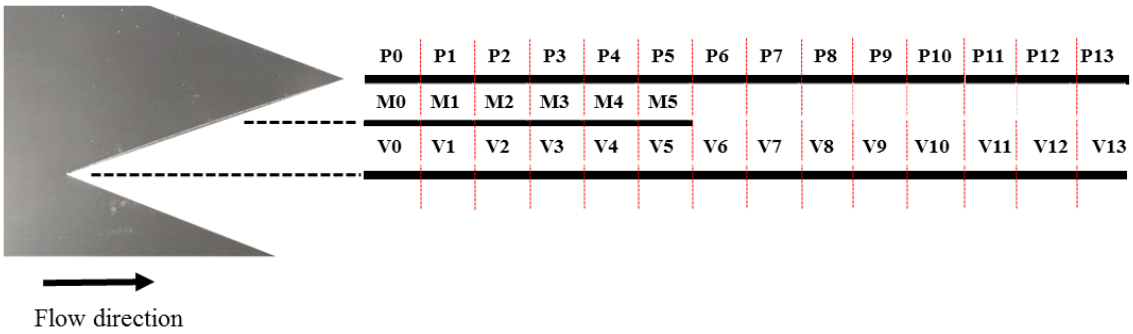

Figure 11: Picture of the all the location where data was collected

Table 4: Test matrix of the conducted tests.

Configuration	Speed	Locations	Collection Range
Peak	0.1 m/s, 0.6m/s, 0.9m/s, 1.2m/s	P0 - P13	260 mm
Valley	0.1 m/s, 0.6m/s, 0.9m/s, 1.2m/s	V0 - V14	260 mm
Mid	0.1 m/s, 0.6m/s, 0.9m/s, 1.2m/s	M0 - M5	120 mm

1.2 1.2 m/s. The color scheme on the far right shows the velocity magnitude. Immediately downstream of the peak, the velocity is almost half the freestream while downstream of the valley has only 10% decrease from the freestream, which illustrates the drastic change in magnitude . Even though the step of the valley is much further upstream than the step of the peak, the peak seems to be more turbulent than the valley at this location. From the velocity vector fields, the boundary layer can be extracted from any streamwise location. An example of a raw boundary layer can be seen in Fig. 13 (a). From this plot alone, not much information can be obtained. First, the free stream velocity needs to be defined as shown by Fig. 13 (b). Given the freestream speed (U_∞), the 99% of (U_∞) can be defined, which is used to determine the 99% BL thickness (δ). Note that linear interpolation of the points intersect $0.99u_\infty$ and the velocity profile were used to determine δ. Using the free stream velocity, a scaled boundary layer profile can be constructed as shown in Fig. 13 (c). A scaled boundary layer profile can then be used to compare between multiple tests, as shown in Fig. 15.

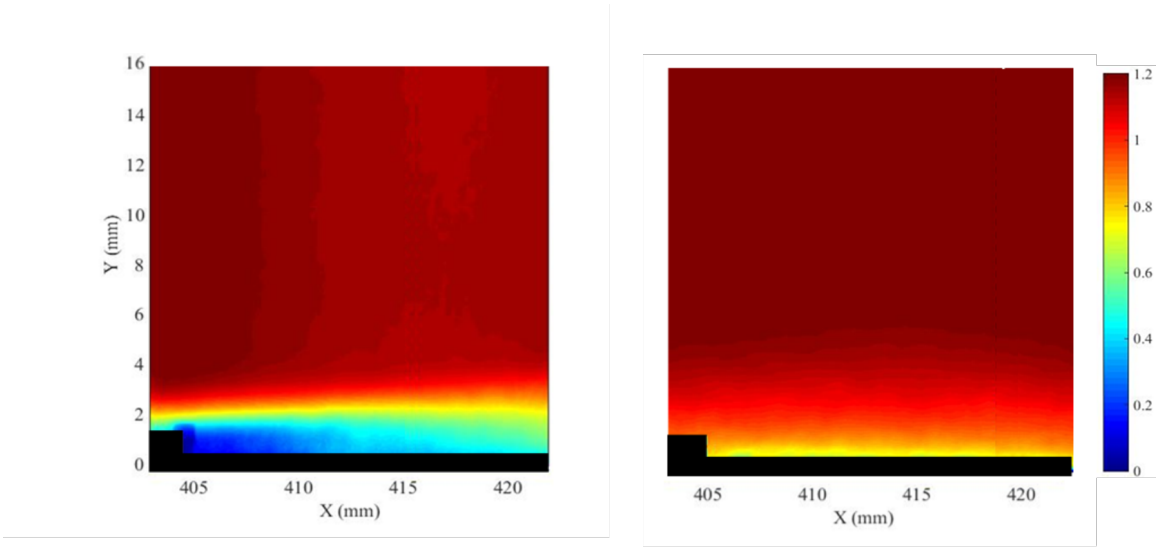

Figure 12: Velocity profiles downstream of (a) peak and (b) valley

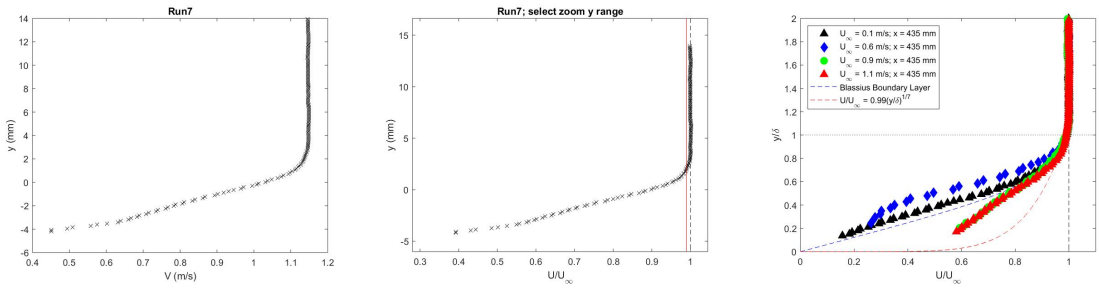

(a) **(b)** **(c)**

Figure 13: (a) raw Boundary layer profile, (b) BL profile with freestream velocity (c) scaled boundary layer profiles

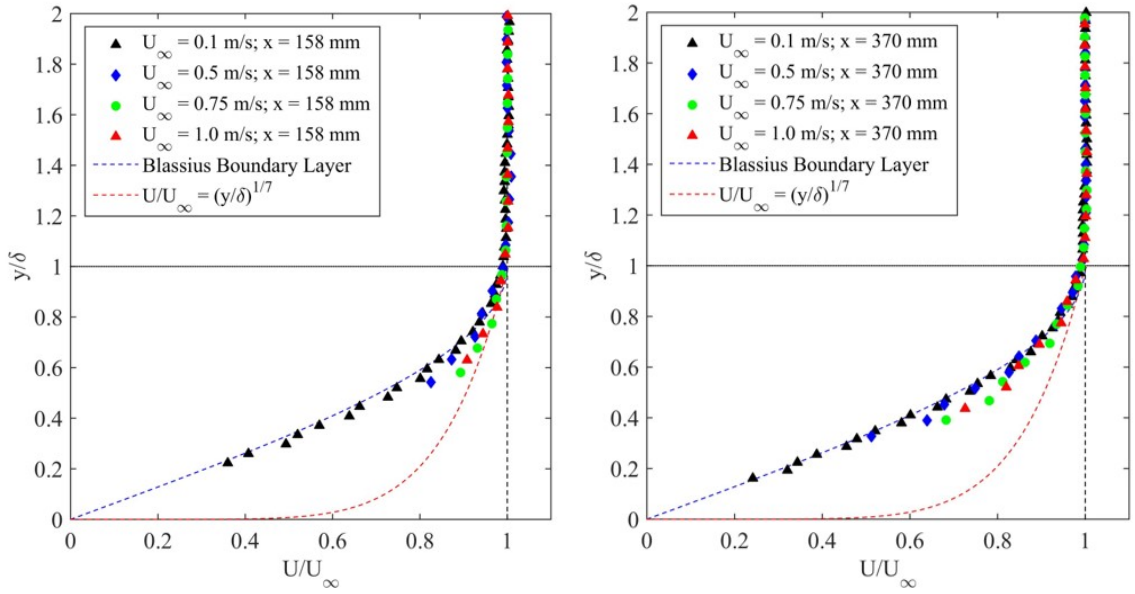

(a) Boundary Layer Profile at x = 158 mm **(b) Boundary Layer Profile at x = 370 mm**

Figure 14: Flat plate boundary layer profile for multiple speeds at : (a) x = 158 mm, (b) x = 370 mm.

4.3. Discussion

Before investigating the boundary layer for CVG configuration, the flat plate by itself was investigated. The flat plate had to be validated before any tests were conducted. The boundary layer was investigated at two locations and 4 different speeds, as shown in Fig. 14. Every single profile that was tested followed the Blasius solution. Therefore, it was be concluded that the flat plate was indeed valid.

Moving on to CVGs and looking at the datasets with the same spanwise location as the location immediately downstream of the peak (Locations P1, V1, and M1), a small region of separated flow can be seen downstream of the peak. Upon reattachment approximately seven step heights away, the flow quickly transitions into a turbulent flow that is given by $U/U_\infty = 0.99(y/\delta)^{1/7}$ for Re_x greater than 100,000. However, this was not the case for the valley or the mid-locations at the same conditions, as the flow remained laminar. Fig. 15 shows the velocity profile approximately 100 mm away from the peak (location P5, V5, and

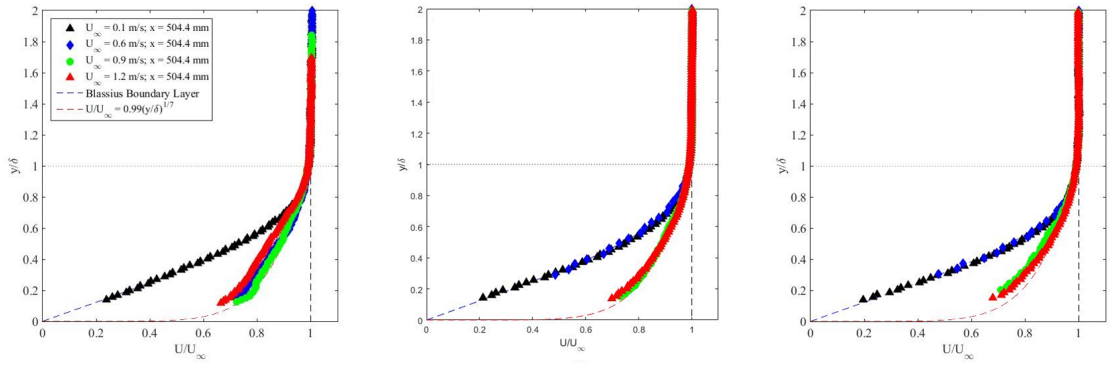

(a) Location P5 (peak) **(b) Location M5 (mid)** **(c) Location V5 (valley)**

Figure 15: Boundary layer velocity profiles downstream of (a) peak, (b) mid, and (c) valley.

M5). The only difference is that the boundary layer at 0.6 m/s is turbulent for peak while it is laminar for both valley and mid-locations.

Fig. 16 shows the momentum thickness downstream of the CVG plotted versus the downstream distance based Reynolds numbers. At lower Reynolds numbers, spanwise variation in the momentum thickness can be seen with the peak transitioning to turbulent earlier than the valley. At high Reynolds numbers, all locations follow the turbulent line. This plot suggests that the transition point downstream of the valley is $Re_x \approx 1.3 \times 10^5$ and less for the mid-locations. The fastest test condition ($Re_H = 1800$, $Re_x = 4.86 \times 10^5$) has the shape of a turbulent boundary layer, as shown by the shape factor plot in Fig. 17. Looking at two CVG lengths downstream of the peak, once again, a persistent spanwise variation can be seen.

4.3.1. Uncertainty Analysis

The calculation of the momentum thickness of the boundary layer required many steps where error propagated along the way. The velocity, U, used for the momentum thickness is an ensemble average of 1000 data points. The fluctuation, ϵ_U, in the the total data set is set to be less than 1%. The freestream velocity, U_∞ was found by observing the

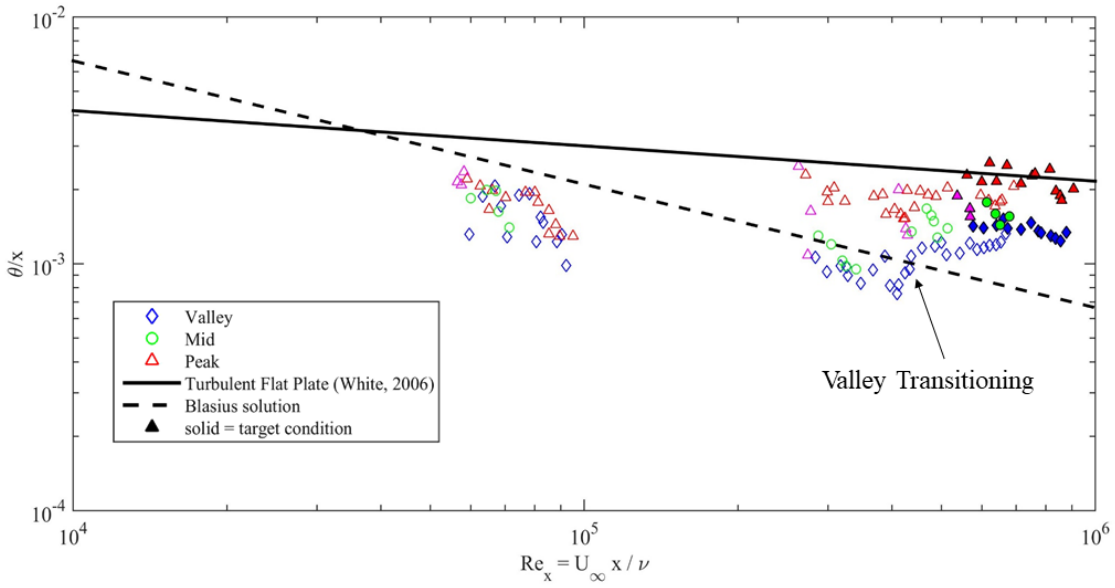

Figure 16: Scaled momentum thickness vs. downstream distance based Reynolds number. For reference, lines corresponding to the momentum thickness for turbulent and laminar and flat plates are shown.

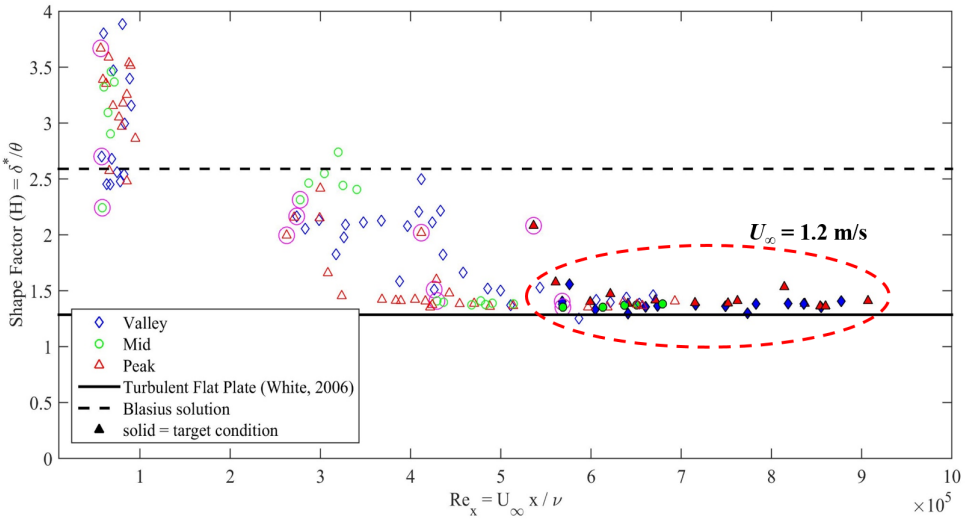

Figure 17: Shape factor plotted vs. downstream distance based Reynolds number. All data was acquired on a flat plate model in a water tunnel. For reference, lines corresponding to the shape factor for turbulent and laminar flat plate are shown.

boundary layer profile of the flow. The error, ϵ_{U_∞}, was estimated to be less than 3%. The boundary layer height, δ, was calculated from the freestream velocity. Therefore, the error, ϵ_δ, was also estimated to be roughly 3%. The following steps were taken to calculate the uncertainty of the momentum thickness. The momentum thickness equation is given as:

$$\theta = \int_0^\infty \frac{U}{U_\infty}(1 - \frac{U}{U_\infty})dy = \delta \int_0^\infty \frac{U}{U_\infty}(1 - \frac{U}{U_\infty})d\eta, \tag{22}$$

where

$$\eta = y/\delta. \tag{23}$$

Now, the uncertainty of $\frac{U}{U_\infty}$, ϵ_{U/U_∞}, can be given as:

$$\epsilon_{U/U_\infty} = \frac{U}{U_\infty}\sqrt{(\epsilon_U)^2 + (\epsilon_{U_\infty})^2} = \frac{U}{U_\infty}\sqrt{(1\%)^2 + (3\%)^2}, \tag{24}$$

and the uncertainty of η, ϵ_η, can be given as:

$$\epsilon_\eta = \eta\sqrt{(\epsilon_y)^2 + (\epsilon_\delta)^2} = \eta\sqrt{(0\%)^2 + (3\%)^2}. \tag{25}$$

For better accuracy, the boundary layer profile can be power fit as the following:

$$\frac{U}{U_\infty} = A\eta^B, \tag{26}$$

which then can be rewritten as:

$$\epsilon_{U/U_\infty} = A\epsilon_\eta^B. \tag{27}$$

The momentum equation can be rewritten as the following:

$$\frac{\epsilon_\theta}{\delta} = \int_0^\infty A\epsilon_\eta^B(1 - A\epsilon_\eta^B)d\epsilon_\eta = \sum_{U=1}^{N} A\epsilon_\eta^B(1 - A\epsilon_\eta^B)d\epsilon_\eta. \tag{28}$$

Using data from one of the conducted tests, the error, $\frac{\epsilon_\theta}{\delta}$, was calculated to be roughly 0.55%. This number is even smaller than the starting value of 3%. This is most likely due to the power fit curve which reduced the inaccuracy of the calculation.

4.4. Conclusions

An experiment investigating the boundary layer of a flat plate with CVG was conducted at the low speed water tunnel facility at Oklahoma State University. The flat was 750 mm long and 300 mm wide. A CVG tape was scaled and installed to the leading edge of the flat plate. The CVGs were 105 mm long and 76 mm wide. The thickness of the tape was 1.48 mm. Particle image velocimetry (PIV) was conducted at multiple locations downstream of the peak and the valley of the CVG. The velocity profiles at different locations were extracted and the boundary layer characteristics were investigated.A number of preliminary conclusions can be drawn from this study. Three primary determinations can be made about the flow physics are:

1. The flat plate was validated as the boundary layer profile followed the Blasius laminar solution at up to 370 mm downstream from the leading edge of the plate.

2. Boundary layer investigation shows that there is clear span wise variation in the velocity distribution. The variation can be seen up to 2 CVG lengths downstream of the peak.

3. The flow downstream of the peak transitions to a turbulent flow earlier than the downstream of the valley. This occurs despite the step of the valley being much further than the step of the peak.

CHAPTER V

EXPERIMENT II: WAKE SURVEY

5.1. Experimental Methods

5.1.1. Facility

The wake survey study was conducted in Oklahoma State University's Flexible-Use Wind Tunnel [20]. The wind tunnel was custom built by Diehl Aero-Nautical. It is an open loop, draw down tunnel that is powered by a 125hp centrifugal fan. The wind tunnel is subsonic with an area contraction ratio of 16:1. The inlet of the tunnel is fitted with 0.3 m (1 ft) long tubes that act as flow straighteners to reduce turbulence in the flow. The test section of the tunnel was 2.44 m (8 ft) long and had a cross section of 0.91 m by 0.91 m (3 ft by 3 ft). The wind speed in the tunnel was variable with a maximum speed of 30.48 m/s (100 ft/s) with the test section empty. Zimbelman [25] showed that the turbulent intensity inside the tunnel was less than 1.4%. A picture of the tunnel and its schematic is provided Fig. 18 [18].

5.1.2. Test Model

The test model that was used for this experiment was an airfoil with an LA203A profile and a chord length of 0.197 m (7.75 in) as shown in Fig. 19. It was designed and manufactured at the University of Kentucky. To build the airfoil, three 0.3 m (12 in) long

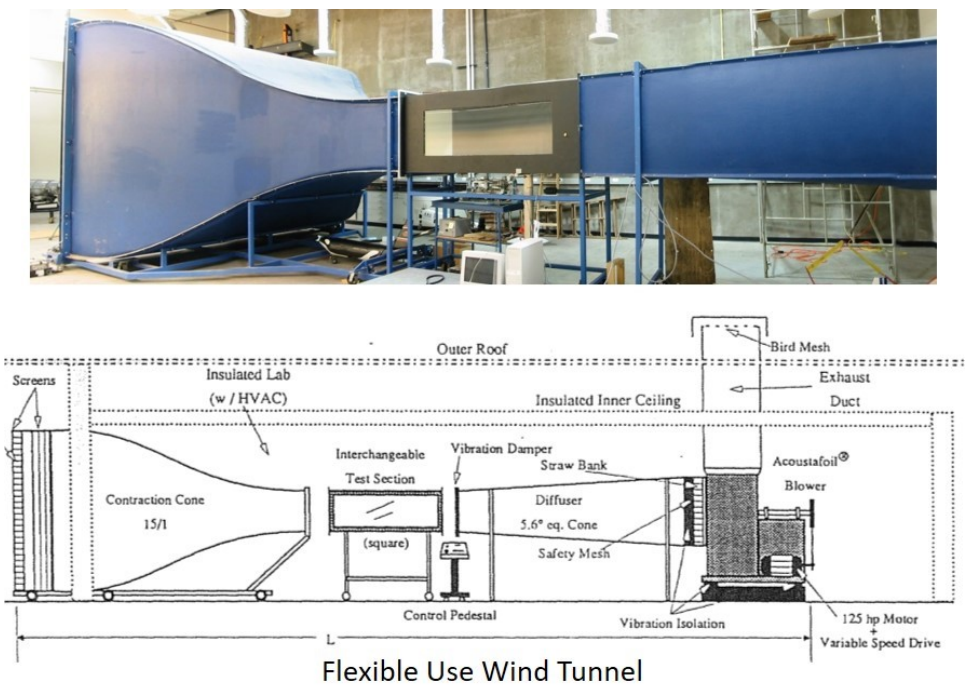

Figure 18: (top) A picture and (bottom) schematic of the Oklahoma State University Subsonic Wind Tunnel [18]

identical pieces were 3D printed. The reason for 3D printing the airfoil separately was to accommodate the size of the 3D printer that was available. The three pieces were then screwed together and epoxied to form a 0.91 m (36 in) long piece.

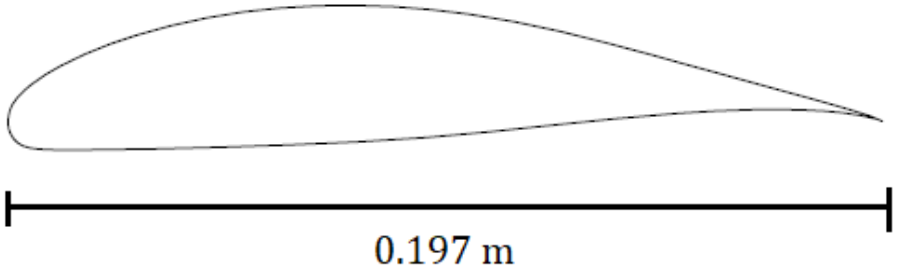

Figure 19: LA203A Wing Profile.

5.1.3. CVG Configurations

Testing was performed in two phases. In the first phase of the wake survey, four different CVG configurations were tested. For simplicity, they will be called CVG-V1,-V2,-V3, and -V4. The CVG-V1 was scaled to be three times the dimensions of the CVGs used on the Boeing 737 aircraft. Therefore, three layers of tape were stacked on top of each other to create CVG-V1 for the wing model. The total thickness of the tape was roughly 1.1 mm. For CVG-V1, the valley was located at 10% chord length. This 10% is significant because this was the chord-wise location of the CVGs on the Boeing 737 aircraft. The distance from peak to peak (width) was 5 cm and the distance from the base to the peak was 7 cm in for CVG-V1. A simple schematic and the picture of the configuration is shown in the top half of Fig. 20.

Fig. 20 (c) shows the picture and dimensions of CVG-V2. For this configuration, the CVG dimensions were half the dimensions of CVG-V1, excluding the tape thickness. Therefore, the distance from peak to peak for CVG-V2 was 2.5 cm, the distance from the base to peak was 3.5 cm, while the tape thickness was kept the same at 1.1 mm. The valley location was also kept the same at 10% chord length. For CVG-V3 and -V4, as shown in Fig. 20 (c), a different tape with similar thickness was used. For faster and easier experimentation, both configurations were applied at the same time on each half of the model. CVG-V3 had the same dimensions was CVG-V2, however, it was shifted downstream so that the peak of CVG V3 would match the peak of CVG-V1. Therefore, the valley was now located at roughly 27% chord length. For CVG-V4, the width was kept the same as CVG-V2 and -V3, but the length was changed to match CVG-V1. Also tested, but not shown in the pictures were backward facing steps. The steps were located at 10%, 27%, and 44% chord lengths. These three locations correspond to the peaks and valleys of the different CVG configurations. This information is summarized in Table 5.

For the second phase of this experiment, a 5-hole probe was used instead of a single-hole Pitot probe. The reason for not testing with the five hole probe initially was that it was

Table 5: Dimensions of the different testing configurations.

							Location [%c]	
CVG	L [cm]	W [cm]	H [cm]	L/W	L/H	W/H	Valley	Peak
Clean Wing	NA	NA	NA	NA	NA	NA	NA	NA
BFS 1	NA	NA	1.1	NA	NA	NA	10	NA
BFS 2	NA	NA	1.1	NA	NA	NA	27.3	NA
BFS 3	NA	NA	1.1	NA	NA	NA	44.5	NA
V1	7	5	1.1	1.38	61.11	44.44	10.0	44.5
V2	3.5	2.5	1.1	1.38	30.56	22.22	10.0	27.3
V3	3.5	2.5	1.1	1.38	34.38	25.00	27.3	44.5
V4	7	2.5	1.1	1.38	68.75	25.00	10.0	44.5

not available at the time of phase one. A total of four configurations were tested for the second phase: clean wing, CVG-V1, and BFS at 10% and 44% chord lengths.

5.1.4. Instrumentation

The wind tunnel was equipped with a Pitot-static probe at the inlet of the test section. This probe was used to measure the free-stream velocity of the wind tunnel test section inlet. Also at the inlet was a hot wire that measured the velocity and turbulent intensity of the tunnel test section. For phase one of this experiment, a Pitot-static tube was mounted to an automated Dantec traverse. Only the streamwise velocity component was measured using this probe. For the second phase, a five hole probe was used to measure the velocity magnitude (V), angle of attack (α), and the angle of slip (β) in the model wake. A schematic of the five hole probe is shown in Fig. 21. The components that can be calculated in the Cartesian coordinates are as follows:

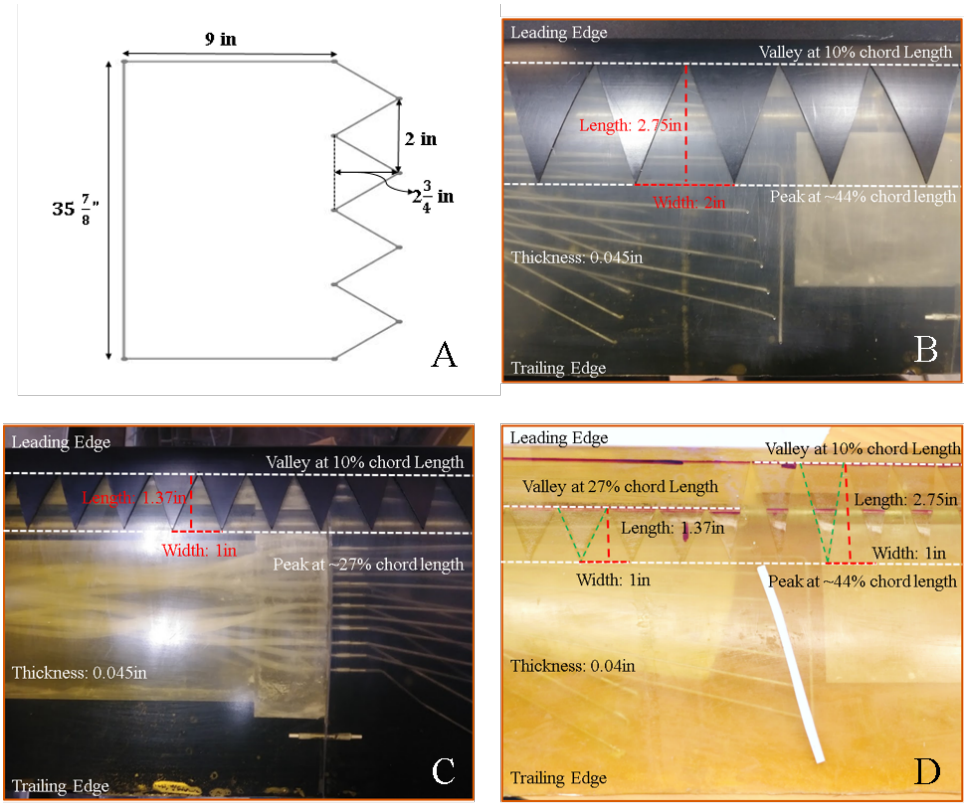

Figure 20: (a) Schematic of CVG V1.0; (b) CVG V1; (c) CVG V2, and (d) CVG V3 and V4.

$$u = V \cos\alpha \cos\beta, \tag{29}$$

$$v = V \sin\beta, \tag{30}$$

$$w = V \sin\alpha \cos\beta. \tag{31}$$

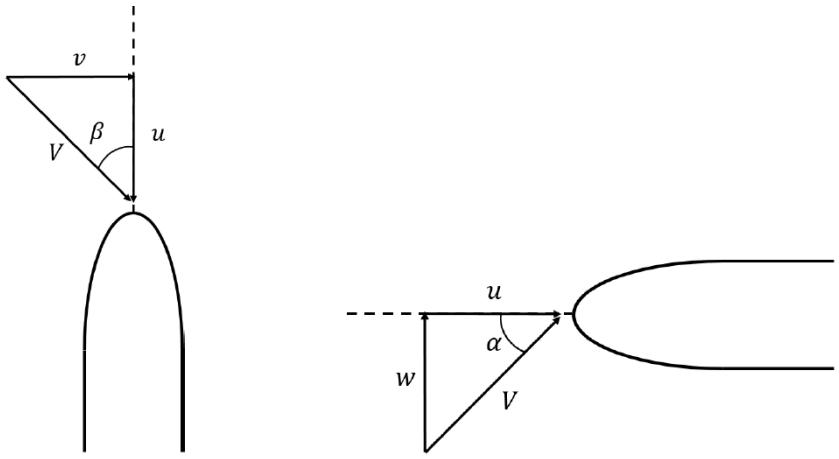

(a) Top view **(b) Profile view**

Figure 21: Schematic of the five hole probe coordinate system and variables.

A National Instruments 9220 analog input card and CDAQ 9188 were used to read the signals into a LabVIEW Virtual Instrument (VI). Fig. 22 shows the test wind tunnel test section with all of the instruments as well as a simple schematic of the DAQ system. Data was sampled at a rate of 1000 Hz and the DC average voltage was taken every 100 samples for an effective sampling rate of 10 Hz. An Extech instruments SD700 barometric pressure temperature data logger was used to measure the ambient air properties at the inlet of the tunnel. These properties were manually input into the VI.

5.1.5. Experimental Method

Quantitative wake survey is one of the methods used to study the aerodynamics of a flow. Lift and drag may be obtained directly from the wake survey using techniques outlined

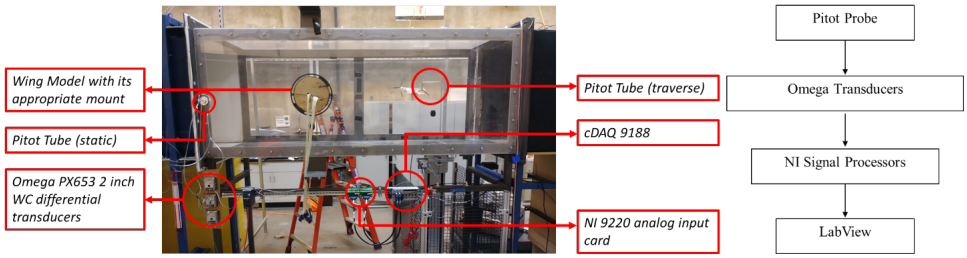

Figure 22: Test section instrumentation and simple schematic of the wake survey system.

in Brune [26]. Conservation of momentum can be used to calculate the drag force on the wing. For wakes, the momentum equation can reduced to

$$\frac{D}{\rho U_\infty^2 b} = \int \frac{U}{U_\infty}(1 - \frac{U}{U_\infty})dy. \tag{32}$$

The relationship of drag force and coefficient of drag, C_D, is given as:

$$D = \frac{1}{2} C_D \rho U_\infty A. \tag{33}$$

Combining Eqs. 32 and 33, the following equation for C_D for the wake of the wing can be found:

$$C_D = \frac{2}{c} \int \frac{U}{U_\infty}(1 - \frac{U}{U_\infty})dy. \tag{34}$$

The velocity profiles of the wake were imported into MATLAB and the C_D values were estimated using MATLAB's trapezoidal rule function. The corresponding wake survey geometry is shown in Fig. 23.

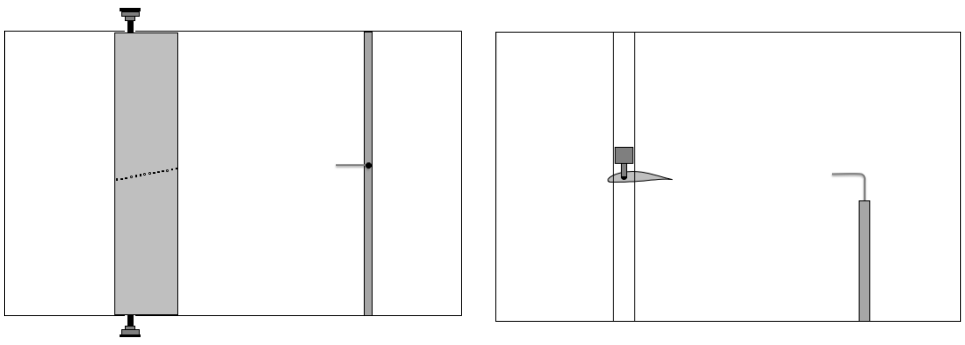

Figure 23: Side and top view of the wake survey system relative to the wing model.

Table 6: Test matrix of the conducted tests

Configuration	AoA Range [$\circ$]	U_∞ [m/s]	Δz [mm]	Δy [mm]	Points
Clean Wing	0 - 10	20, 26	25	3.18	$\sim$ 100
BFS	0 - 10	20, 26	25	3.18	$\sim$ 100
CVG	0 - 10	20, 26	12.5	3.18	$\sim$ 100

5.1.6. Test Matrix

The wing model was fixed at 0.762 m downstream from the inlet of the test section. It is important to note that the probe head was roughly 5 chord lengths downstream from the model itself. Tests were conducted at roughly 20 and 26 m/s. The chord length based Reynolds number for these velocities were approximately 230,000 and 300,000, respectively. Multiple angles of attack were tested for each operation condition, ranging from 0 to 10 degrees. For the CVG configurations, the spanwise increment on the traverse was set so that it was positioned to take data directly downstream of both peaks and valleys separately. For the clean wing and backwards facing step configurations, the spanwise increment was set to 2.5 cm. The vertical increment was set to half of the diameter of the probe head (3.18 mm) in order to get optimal resolution for the wake deficit. The final matrix is shown in Table 6.

5.2. Results

From the wake survey, a raw velocity profile of the wake at a single spanwise location is shown in Fig. 24 (a). The lowest of the velocity represents the point of largest wake deficit, while the highest velocities are the free stream velocities of the flow. Qualitatively, not much can be obtained from this plot. However, quantitatively, the coefficient of drag can be calculated from this data and will be analyzed in the discussion section. To compare the data qualitatively, more wake profiles need to be plotted. When multiple profiles are

plotted on the same graph, it typically looks similar to like Fig. 24 (b). This plot is even more confusing. Therefore, a new approach to plotting wakes was needed. A contour plot fits the need of plotting the wake profiles and an example is shown in Fig. 26 (a).

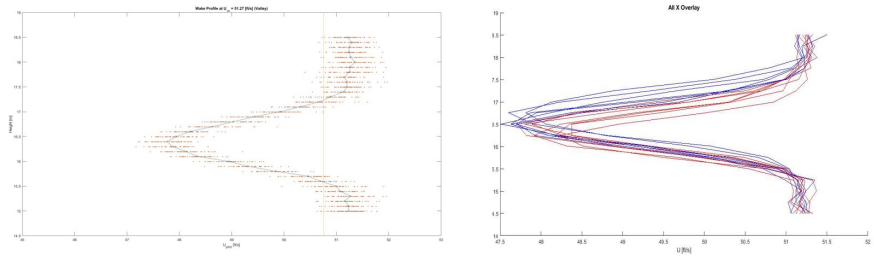

Figure 24: (a) Raw wake profile from a single spanwise location, (b) raw wake profiles from multiple spanwise locations.

5.3. Discussion

5.3.1. Clean Wing

The results for both speeds were very similar, as shown by Fig. 25, therefore, only the results of the higher speed tests will be shown moving forward. The results of the clean wing is shown in Fig. 26. Fig. 26 (a) shows the contour plot of the clean wing wake 5 chord lengths downstream. The abscissa shows the span wise location of the wake while the ordinate shows the scaled half-deficit of the wake. The half-deficit of the wake is the location in the ordinate where the wake deficit is exactly half of the maximum wake deficit. The colors represent the streamwise speed of the flow as shown in the color bar to the right of the plot. Yellow represents the freestream speed and the darkest of blue represents the largest wake deficit. Qualitatively, the wake deficit, can be observed by the intensity of the color blue. As expected, the plot shows that there is not significant spanwise variation in the deficit for the clean wing.

To represent the wake deficit quantitatively, coefficient of drag, C_D, was calculated and plotted. Fig. 26 (b) shows the C_D plot for the clean wing at Re = 300,000 and is

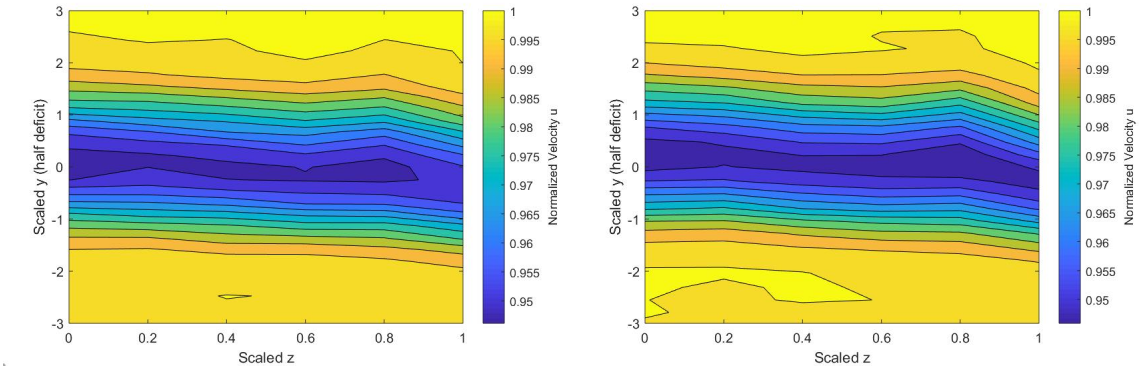

(a) Re **= 230,000** **(b)** Re **= 300,000**

Figure 25: Velocity u for clean wing at 0 degrees angle of attack: (a) Reynolds number of 230,000 (b) Reynolds number of 300,000

compared to the C_D plot of the same airfoil from Xfoil simulations. The angle of attack of the wing is on the abscissa and the coefficient of drag is shown on the ordinate. The C_D values for the clean wing and the Xfoil seem to match well for both test conditions at low Reynolds numbers. However, the data does not seem to agree at higher angles of attack. It is important to note that the stall angle for this wing is at 10.25 degrees. The discrepancy between experimental data and the Xfoil simulated results may arise from the fact that simulations are not designed to work with high accuracy when flow separation occurs. Therefore, it is wise to proceed with caution when comparing data at high angles of attack.

5.3.2. Backward facing step

The second experiment was conducted with multiple backward facing steps (BFS). Fig. 27 (a) shows the contour plot of a BFS at 27% chord length. Once again, since there was no span wise variation in the geometry, there is no spanwise variation in the velocity distribution. The plots for the other BFS were very similar to the one shown; therefore, they are not included here. Although their velocity distribution look very similar, their C_D values varied, as shown in Fig. 27 (b). As expected, the C_D for all three BFSs were larger

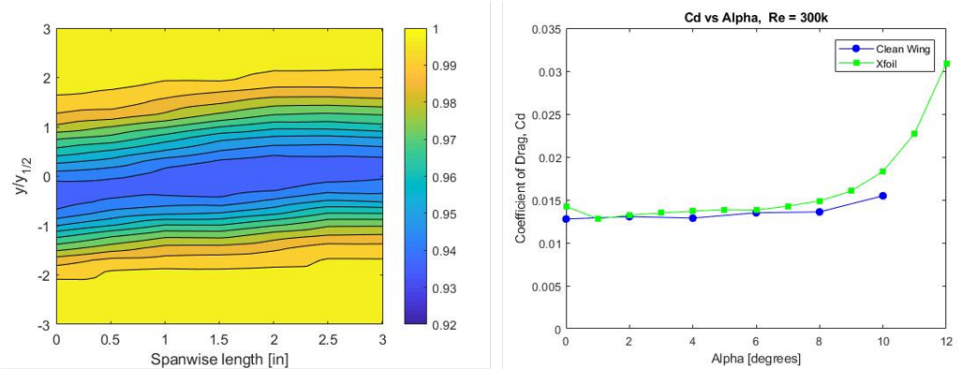

Figure 26: (a) Contour plot of wake at Reynolds number of 300,000 for the clean wing; (b) C_D of the clean wing with Xfoil estimation.

than the clean wing. This was because the thin tape layer added some thickness to the wing. After starting with similar C_D at zero degree angle of attack, the BFS at 10% chord length had the largest C_D of the three with the largest deviation occuring at higher angles of attack. This is because the flow over the step has a higher potential to separate at higher angles of attack. It seems that further upstream the step was, larger the Cd was at higher angles of attack.

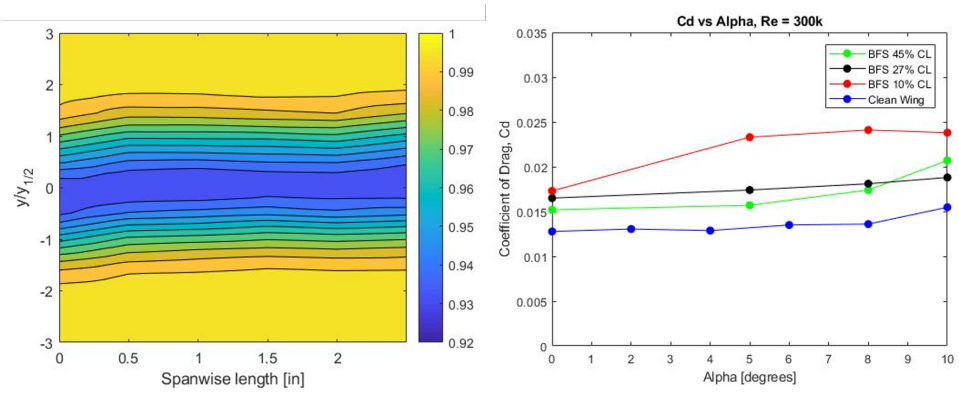

Figure 27: (a) Contour plot of wake at Reynolds number of 300,000 for BFS at 27% chord length; (b) C_D plots of the BFS plotted against the angle of attack and compared with the clean wing.

5.3.3. CVG

The third experiment of phase one was conducted with the different CVG configurations. Fig. 28 shows the contour plot of the model wake with CVG-V1 at Reynolds number of 300,000. The ordinate shows the vertical distance thickness scaled with the half deficit, but unlike the previous two contour plots, the abscissa is now scaled with respect to CVG width. Unlike the first two contour plotss, this plot shows a consistent spanwise variation in the velocitiy distribution. Recall that this wake survey was acquired approximately five chord lengths downstream of the model. At this location, flow was expected to be well mixed and have minimal spanwise variation. However, this was clearly not the case.

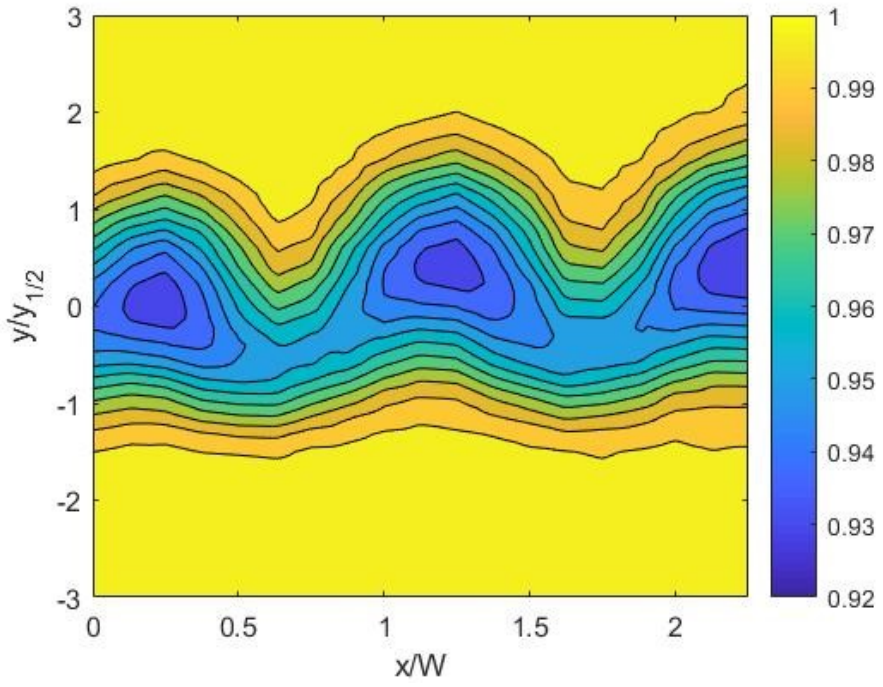

Figure 28: Contour plot of the wake 5 chord lengths downstream of the model at Reynolds number of 300,000 with CVG-V1. The origin of the abscissa lined up with the mid-location between a peak and valley.

Fig. 29 (a) shows the contour plot for CVG-V2. Recall that the peaks and valleys were half of the size of CVG-V1, while the thickness was kept the same. Unlike the first

CVG configuration, there does not seem to be much spanwise variation for CVG V2, even though there was a span wise variation in the model geometry. This plot seems to be more similar to the clean wing than CVG-V1, showing evidence that the structures that were present for CVG-V1 were weaker and consequently did not remain as coherent this far downstream. The plots for CVG-V3 and -V4 were very similar to CVG-V2, therefore, are not included here.

Fig. 29 (b) plots C_D for all of the CVG configurations along with the clean wing. All of the CVG configurations have similar C_D at 0 degree angle of attack. An uncertainty analysis was done using the methods mentioned in the uncertainty section. Using the 10% uncertainty found, the difference in the C_D values at 0 degree angle of attack were found to be negligible. However, when the angle of attack was increased, they all deviate from each other. It is clear that the C_D for CVG-V1, -V2, and -V4 are much higher than CVG-V3 at high angles of attack. This is because the valley for those three configurations were located at 10% chord length while CVG-V3 had its valley further downstream at 27% chord length, providing further evidence that the location of the step a significant impact on performance.

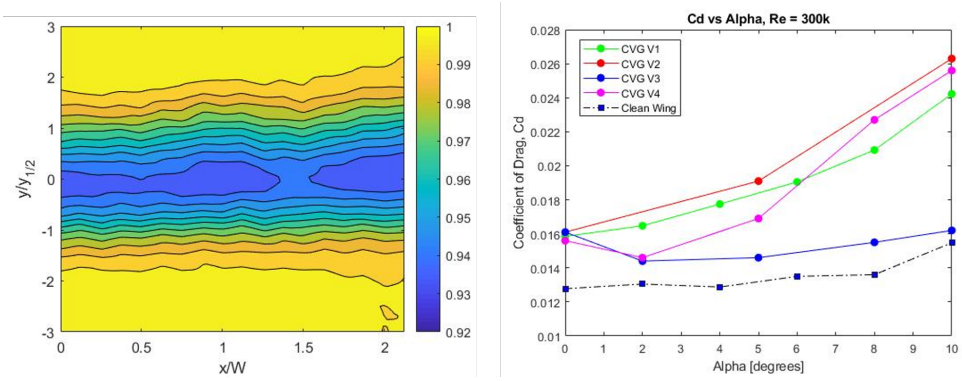

Figure 29: (a) Contour plot of wake at Reynolds number of 300,000 for CVG V2; (b) C_D plots of all of the CVG configurations plotted against the clean wing.

5.3.4. Phase II

For phase II of the wake survey study, a 5-hole Pitot probe was used instead of a single-hole probe. The reason for the use of the 5-hole probe was to capture the 3D flow field of the wake. Instead of a single velocity component (u), all three velocity components (u, v, and w) were measured, as shown in the top row of Fig. 30 from the clean wing at 0° angel of attack. The streamwise velocity, u, is shown in Fig. 30a, which looks as expected and is very similar to to that observed in the phase I clean wing test(Fig. 26a). The corresponding v and w components of the velocity are shown in Fig. 30b and 30c, respectively. A small spanwise variation seems to be apparent in both components, but the magnitude is so small (less than 0.02% of the U_∞) that they are insignificant. The variation may have also arise from the fact that the values in between data points were interpolated and are not direct measurements. Fig. 31a shows the contour plot of the u component v and w vectors superimposed over the contour plot at the same operating condition. The top half of the wake is flowing in the opposite direction than the bottom half. It is important to note that there is no spanwise variation and the vectors are nearly constant across the span of the distribution. Fig. 31b plots the vorticity of the flow. The color bar to the right indicates the intensity of the vorticity. As expected, the observed range does not have much variation with the full range only spanning nominally -10 to 10 $1/s$.

The middle row of Fig. 30 plots the three velocity components for the clean wing at an angle of attack of 4 degrees. These were plotted to show the impact of changing angle of attack on the same configuration. The velocity distribution look very similar between the two angles of attack. The only noticeable difference is that the wake deficit has increased for the four degree angle of attack. Both the vector plot and the vorticity plot are shown in the middle row of Fig. 31 and they look very similar to the previous condition. Once again, the observed range of vorticity only spans nominally -10 to 10 $1/s$.

Similarly, the bottom row of Fig. 30 provides contour plots of the three velocity components for clean wing at an angle of attack of 8 degrees. However, the u velocity

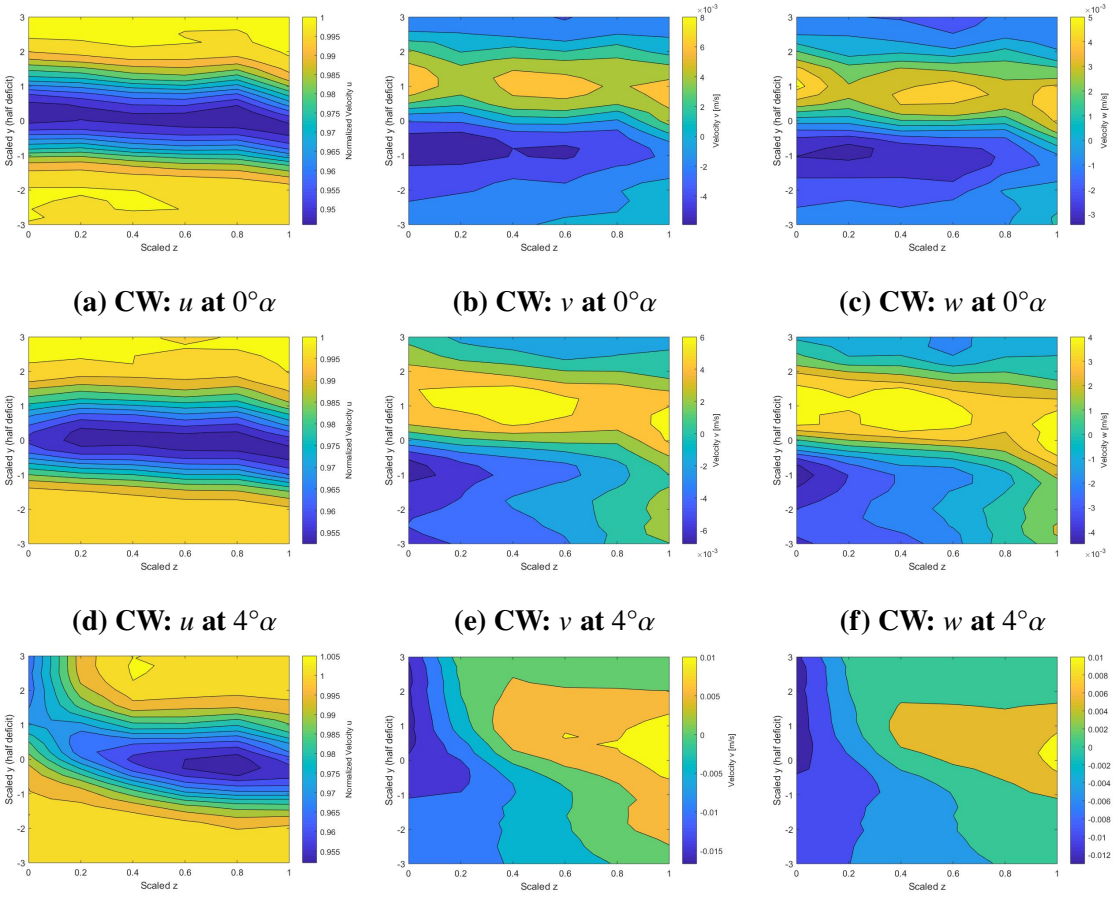

(a) CW: u at $0°\alpha$ **(b) CW: v at $0°\alpha$** **(c) CW: w at $0°\alpha$**

(d) CW: u at $4°\alpha$ **(e) CW: v at $4°\alpha$** **(f) CW: w at $4°\alpha$**

(g) CW: u at $8°\alpha$ **(h) CW: v at $8°\alpha$** **(i) CW: w at $8°\alpha$**

Figure 30: Contour plots of the (left column) u, (middle column) v, and (right column) w velocity components at (top row) $0°$, (middle row) $4°$, and (bottom row) $8°$ angle of attack for the clean wing. All data acquired at Re = 300,000.

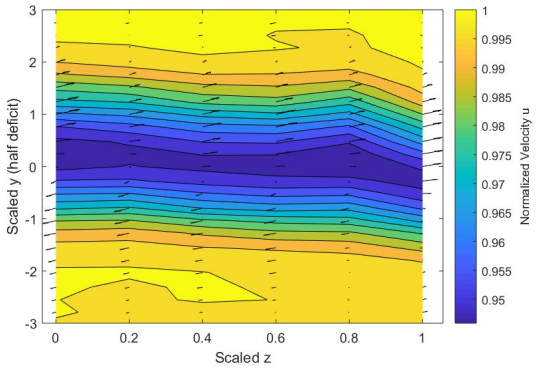

(a) CW: Magnitude of v and w at $0°\alpha$

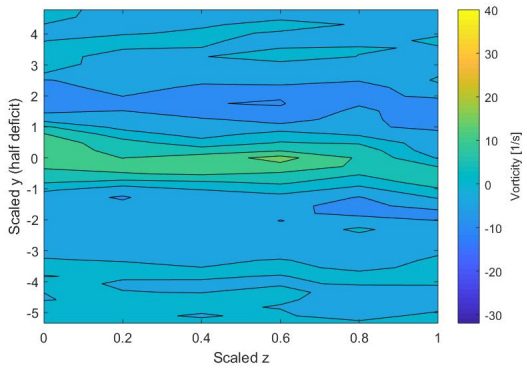

(b) CW: Vorticity at $0°\alpha$

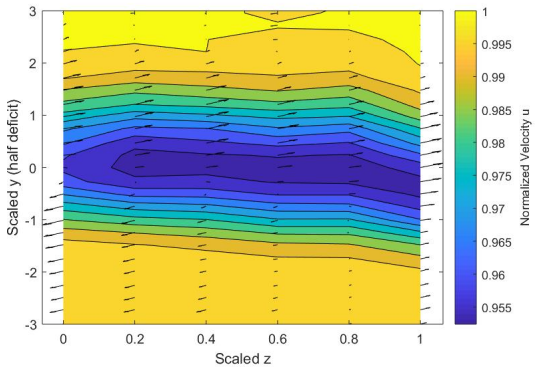

(c) CW: Magnitude of v and w at $4°\alpha$

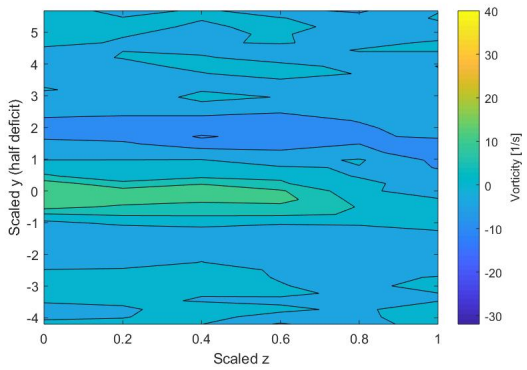

(d) CW: Vorticity at $4°\alpha$

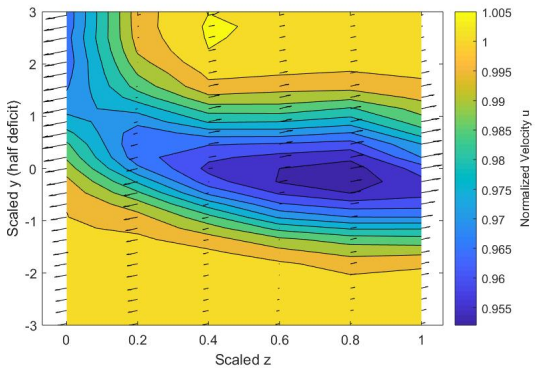

(e) CW: Magnitude of v and w at $8°\alpha$

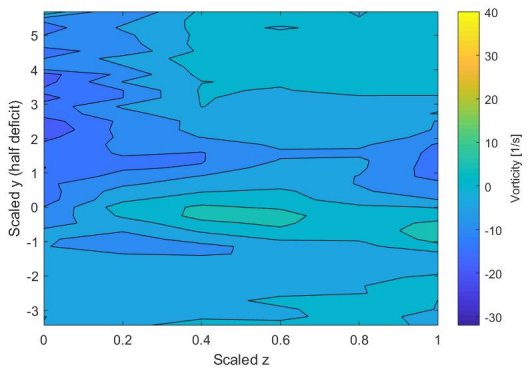

(f) CW: Vorticity at $8°\alpha$

Figure 31: (Left column) Magnitude plot and (right column) vorticity plot of the clean wing at (top row) $0°$, (middle row) $4°$, and (bottom row) $8°$ angle of attack. All data acquired at Re = 300,000.

shown in Fig. 30g looks much different than the previous two. The left side of the wake seems to be bent upward. This is most likely due to of flow separation at high angles of attack. Although, theoretically, the separation for this wing occurs at an angle of attack of 10.25 degrees, it is not surprising that the separation occurred earlier experimentally. This is most likely due to the surface roughness of the model getting worse over time due to its usage, especially with application of CVGs and BFSs that left remnant of epoxy. The separation also seems to have influenced the v and w components as seen in Fig. 30h and 30i. The vector plot shown in Fig. 31e is also different from the previous two as the vectors in this plot seem a bit random. The vorticity, however, as shown in Fig. 31f, looks very similar to the previous two angles of attack. The vorticity seems to have remained the same and still only spans nominally -10 to 10 $1/s$.

Fig. 32 plots the three velocity components s for backward facing step located at 10% and 45% chord length at 0 degree angle of attack. As expected, these look very similar to the clean wing plots at 0 degrees. There is negligible spanwise variation in the flow, as indicated by the vector plots in Fig. 33a and Fig. 33c. The vorticity plots shown in Fig. 33b and Fig. 33d also look very similar to the clean wing. The vorticity still only spans nominally -10 to 10 $1/s$.

Shown in the top row of Fig. 34 are the velocity profiles of CVG-V1 at 0 degree angle of attack. Once again, the velocitiy distribution for this configuration is much different than the clean wing and BFS configurations. The u velocity profile shown in Fig. 34a is almost identical to the one shown in Fig. 28 from the single hole probe. Once again, the presence of strong coherent structures is apparent from the significant spanwise variation that occurs with the CVG spanwise spacing. Recall that the 5-hole probe is roughly 5 chord lengths downstream from the trailing edge of the wing. The wake this far downstream of the wing was expected to be well mixed but once again, a clear spanwise variation persists in the flow. The presence of the coherent structures can also be seen in the v and w velocity profiles, as shown in Fig. 34b and 34c. The vector plot shown by Fig. 35a is also very different

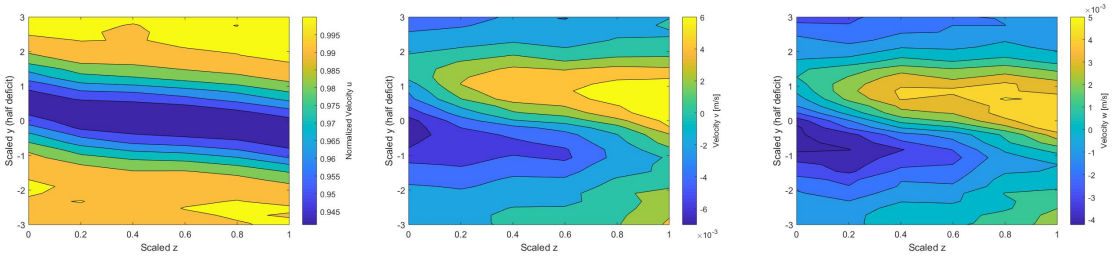

(a) BFS 10%: u at 0° **(b) BFS 10%: v at 0°** **(c) BFS 10%: w at 0°**

(d) BFS 45%: u at 0° **(e) BFS 45%: v at 0°** **(f) BFS 45%: w at 0°**

Figure 32: Contour plots of the (left column) u, (middle column) v, and (right column) w velocity components of (top row) BFS at 10% and (bottom row) BFS at 45%. All data acquired at Re = 300,000 and 0° angle of attack.

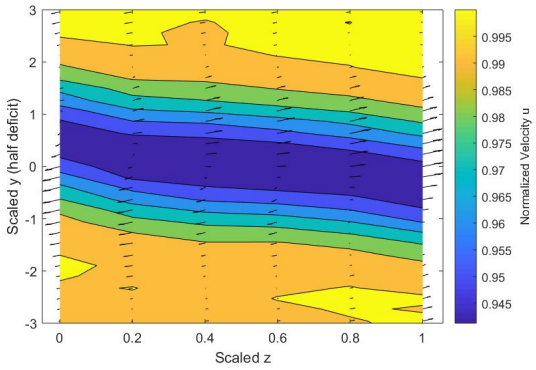

(a) BFS 10%: Magnitude of v and w at 0°

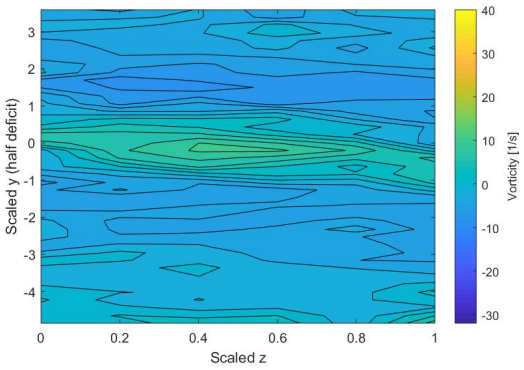

(b) BFS 10%: vorticity at 0°

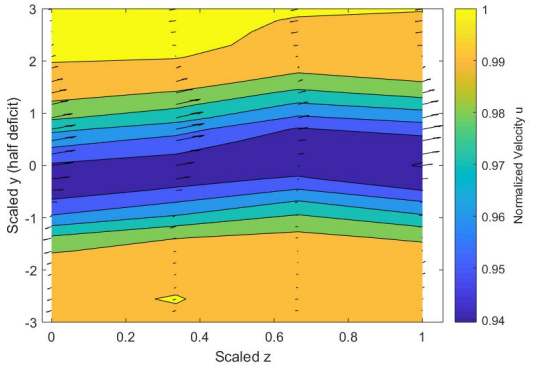

(c) BFS 45%: Magnitude of v and w at 0°

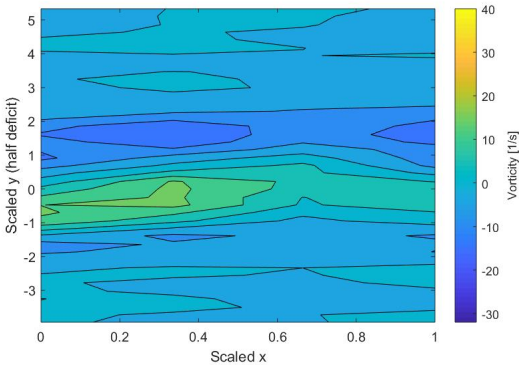

(d) BFS 45%: vorticity at 0°

Figure 33: (Left column) Magnitude plot and (right column) vorticity plot of the (top row) BFS at 10% and (bottom row) BFS at 45%. All data acquired at Re = 300,000 and 0° angle of attack.

from the plots for the Clean wing and BFS. First of all, there is a clear spanwise variation as mentioned above. Second, the region around the largest wake deficits have flows going in the opposite direction. Above the deficit, flow seems to be moving to the right, while below the deficit, the flow seems to be moving to the left. Between the multiple structures, a region of 0 velocity in the y and z region can be seen. This is strong evidence that the CVGs are inducing rotation in the flow. The vorticity plot in Fig. 35a shows that not only there is rotation in the flow, but the rotation is strong with a range of -30 to 40 $1/s$. Also note that the vortices appear to be co-rotating (i.e. each vortex is rotating in the same direction about the local maximum wake deficit). The vorticity plot also shows the vorticity to be skewed, which indicates the possibility that they are rotating about each other.

The middle row of Fig. 34 and the bottom row of Fig. 34 plot the velocity components for CVG V1 at 4 degrees and 8 degrees angle of attack, respectively. For 4 degrees, the strong coherent structures still seem to be there. However, for 8 degrees, the structures seem to have faded away. This is also evident in the vector plots and the vorticity plots shown in left side of Fig. 35 and the right side of Fig. 35, respectively. The vectors in the vector plot are lesser in magnitude and the intensity of the vorticity are also lesser than that of 0 degrees.

The data for phase II was compared quantitatively through an average vorticity plot shown in Fig. 36. The average vorticity was calculated by using the magnitude of the vorticity values within the wake of the different configurations. At quick glance, a general trend can be seen. For relatively low angles of attack, the average vorticity is decreasing as the angle of attack is increasing. However, at high angles of attack, the average vorticity is increasing as the angle of attack is increasing. The higher vorticity is most likely due to the effects of turbulence at higher angles of attack. Overall, the average vorticity is higher for the CVG-V1 than any other configuration. This is evidence that the CVG induces relatively high intensity vorticity on to the flow.

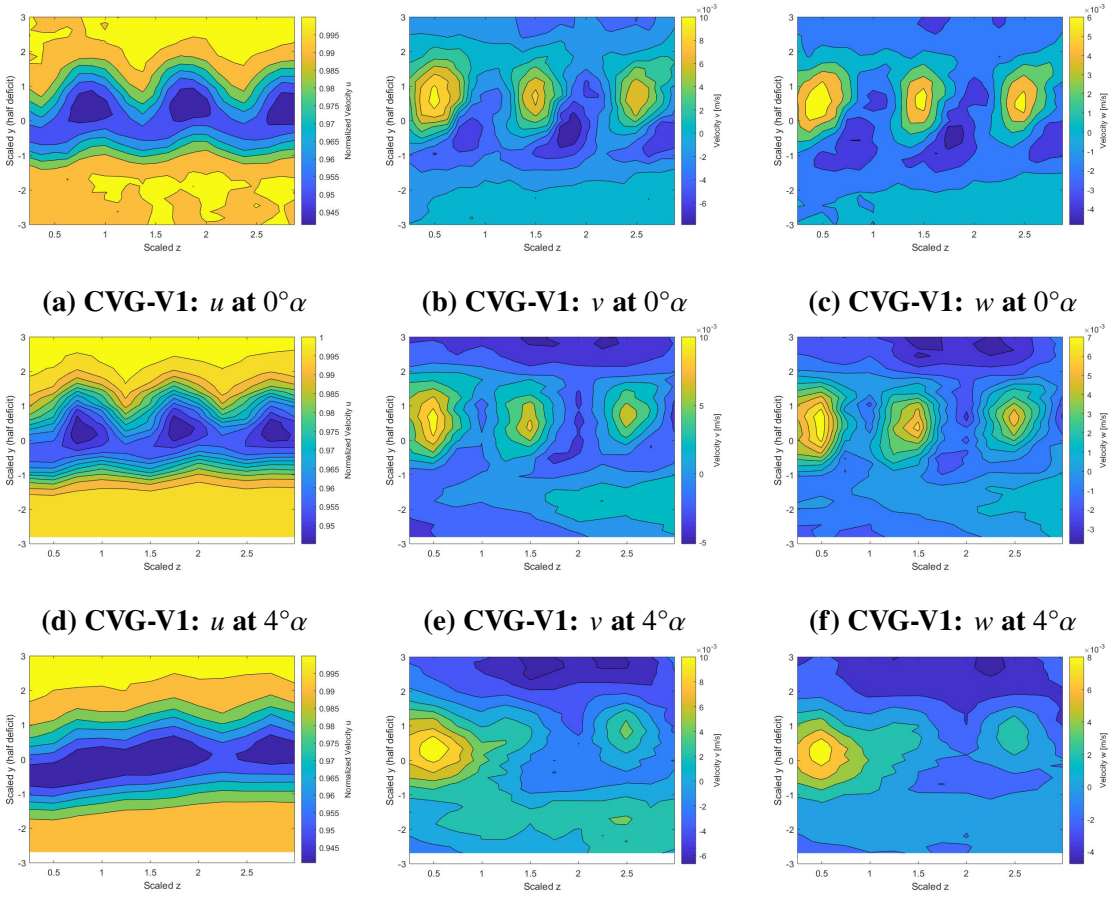

(a) CVG-V1: u at $0°\alpha$ **(b) CVG-V1: v at $0°\alpha$** **(c) CVG-V1: w at $0°\alpha$**

(d) CVG-V1: u at $4°\alpha$ **(e) CVG-V1: v at $4°\alpha$** **(f) CVG-V1: w at $4°\alpha$**

(g) CVG-V1: u at $8°\alpha$ **(h) CVG-V1: v at $8°\alpha$** **(i) CVG-V1: w at $8°\alpha$**

Figure 34: Contour plots of the (left column) u, (middle column) v, and (right column) w velocity components at (top row) $0°$, (middle row) $4°$, and (bottom row) $8°$ angle of attack for CVG-V1. All data acquired at Re = 300,000.

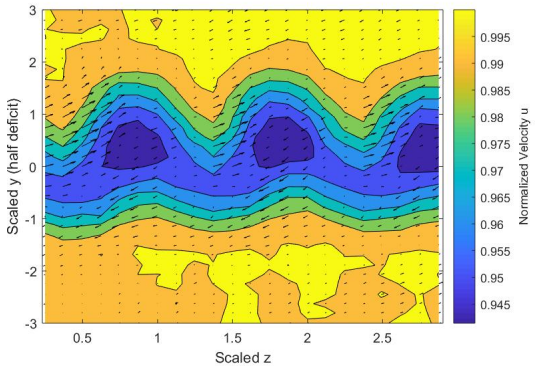

(a) CVG-V1: Magnitude of v and w at $0°$

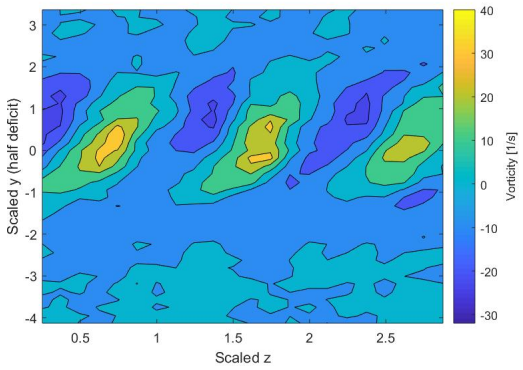

(b) CVG-V1: Vorticity at $0°$

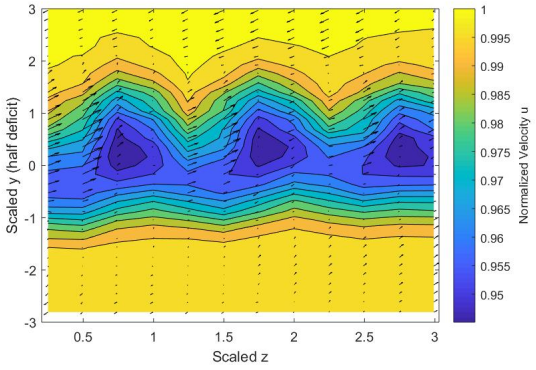

(c) CVG-V1: Magnitude of v and w at $4°$

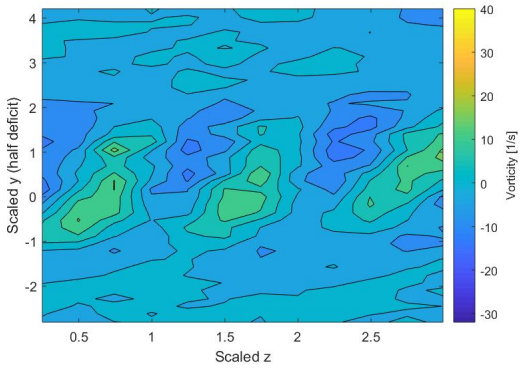

(d) CVG-V1: Vorticity at $4°$

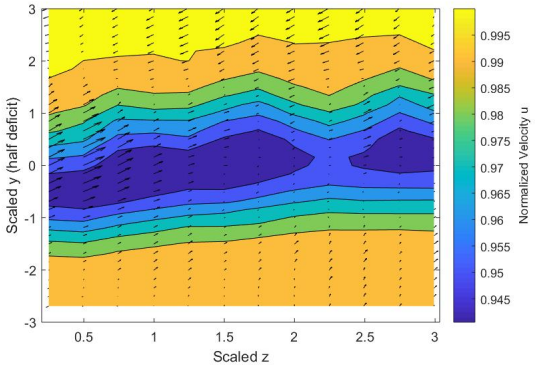

(e) CVG-V1: Magnitude of v and w at $4°$

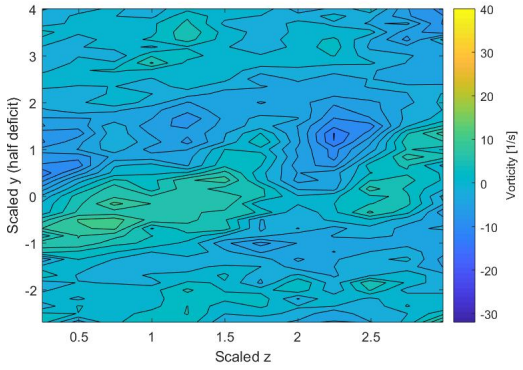

(f) CVG-V1: Vorticity at $8°$

Figure 35: (Left column) Magnitude plot and (right column) vorticity plot of CVG-V1 at (top row) $0°$, (middle row) $4°$, and (bottom row) $8°$ angle of attack. All data acquired at Re = 300,000.

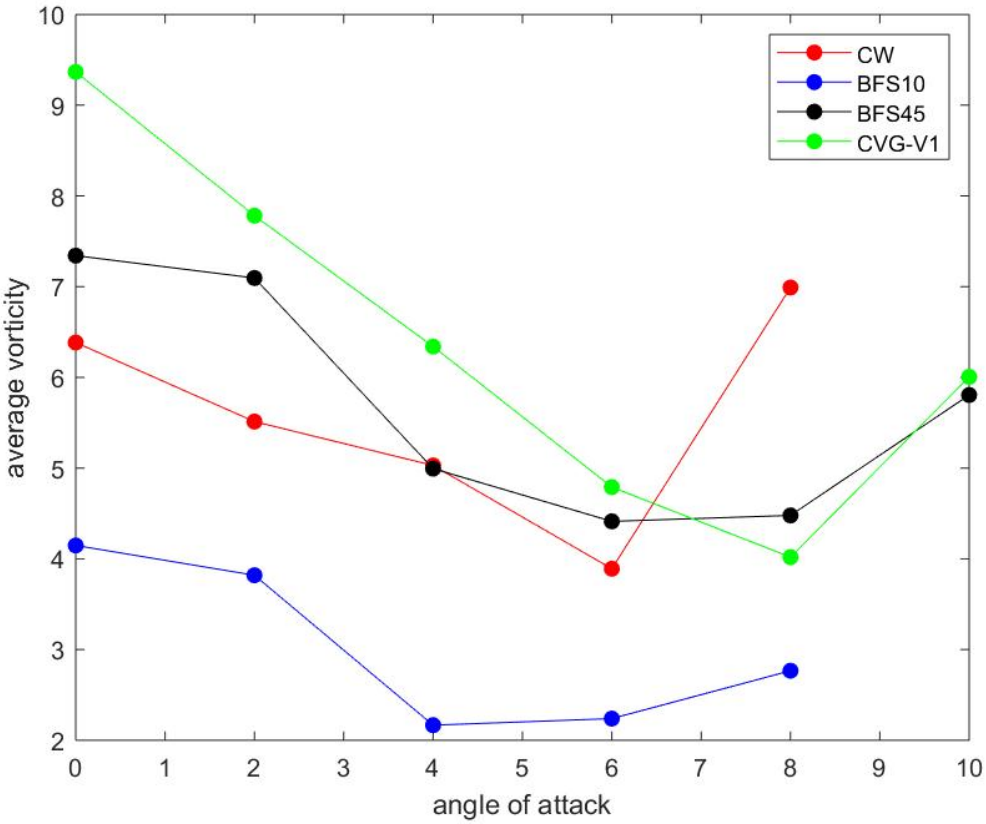

Figure 36: Average vorticity for the wake of all the configurations

5.3.5. *Phase I and II comparison*

Fig. 37 compares the coefficient of drag between phase I and II for the clean wing and CVG V1 configurations. As previously stated, the C_D values for the CVG for both phase I and II are larger than that of the clean wing. However, the difference in the C_D values between phase I and II for both the configurations are minimal. More analysis is shown in the uncertainty section.

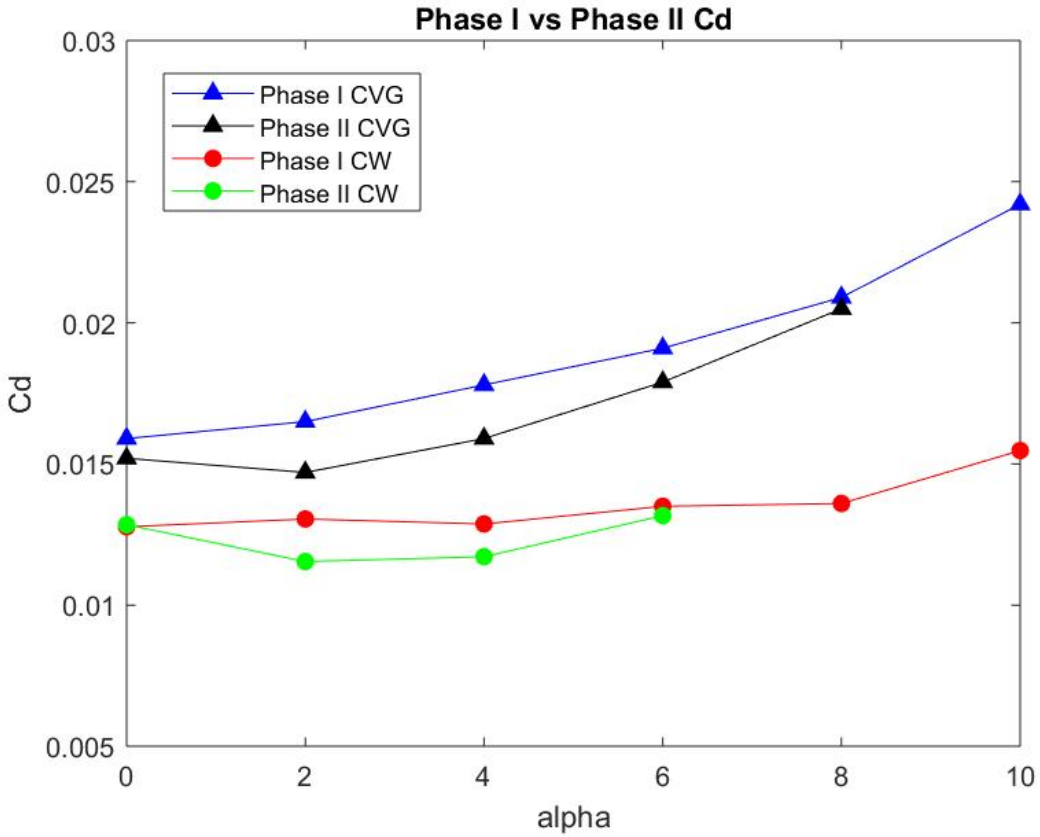

Figure 37: Comparison of clean wing and CVG-V1 between phase I and II

5.3.6. *Uncertainty Analysis*

Uncertainty of the Coefficient of Drag

Like the momentum thickness in the boundary layer investigation, the coefficient of drag is also calculated in many steps. The errors in the first few step propagate down and

create a larger uncertainty in the C_D values. Instead of estimating the percent error, the uncertainty was calculated using the standard deviation, σ , of the collected datasets. The following steps were taken to find the uncertainty of the coefficient of drag: The coefficient of drag, C_D is given by:

$$C_D = \frac{2}{c}\int \frac{U}{U_\infty}\left(1 - \frac{U}{U_\infty}\right) dy \tag{35}$$

Now, the uncertainty of $\frac{U}{U_\infty}$, σ_{U/U_∞}, can be given by:

$$\sigma_{U/U_\infty} = \frac{U}{U_\infty}\sqrt{\left(\frac{\sigma_U}{U}\right)^2 + \left(\frac{\sigma_{U_\infty}}{U_\infty}\right)^2}. \tag{36}$$

Therefore, the $\frac{U}{U_\infty}$ in the C_D equation can be replaced by σ_{U/U_∞} as the following:

$$C_D = \frac{2}{c}\int \sigma_{U/U_\infty}\left(1 - \sigma_{U/U_\infty}\right) dy \tag{37}$$

Using the equation above, the uncertainty of a C_D was calculated to be about ±10%. Fig. 38 shows the C_D plot of a run with error bars.

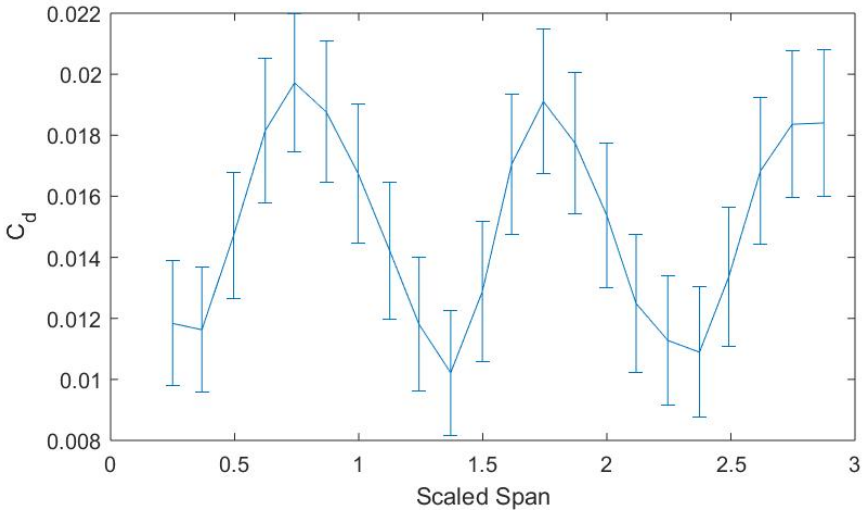

Figure 38: Uncertainty of C_D at across the CVG.

Phase I and Phase II comparison

The uncertainty of 10% can also be used to compare the drag coefficient between phase I and Phase II. The 10% uncertainty can be applied to Fig. 37, and the uncertainty plot

is shown by Fig. 39. This figure shows the difference in the coefficient of drag with error bars versus angle of attack between phase I and phase II for the clean wing and CVG-V1. As shown by this figure, the difference in C_D between phase I and II are minimal. The uncertainty regions between phase I and II overlap other, meaning that the actual value might fall anywhere in that region. Therefore, it can be concluded that the phase I and II data sets were similar and the differences were negligible.

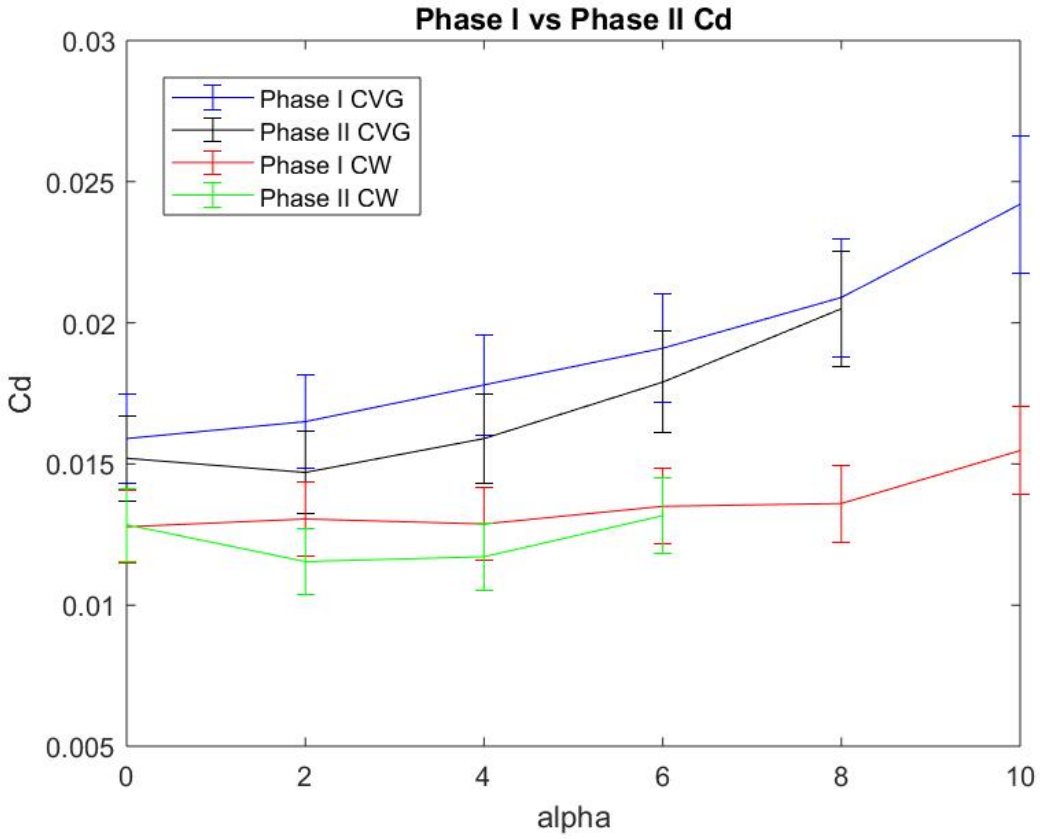

Figure 39: Comparison of clean wing and CVG-V1 between phase I and II with error bars

5.4. Conclusions

A wake survey study was conducted at the subsonic wind tunnel at Oklahoma State University. A wing model with an LA203A profile was used for this study. The model had

a chord length of 7.75 in and was 36 in wide. Clean wing, three backwards facing steps, and 4 CVG configurations were tested for this study. The thickness of the tape was 1.1 mm. For the first phase of the study, a single hole pitot-static probe was use to measure the stream wise velocity of the flow in the downstream wake region of the wing. From this study, velocity profiles were extracted and the coefficient of drag was calculated for all configurations. For the second phase of the study, A 5-hole probe was used to capture all three velocity components of the flow. The following conclusions can be drawn from the study:

5.4.1. Phase I

1. The CVG generates strong coherent turbulent structures that persist into the far wake region even at five chord lengths downstream of the wing;

2. Making the CVG sizes smaller weakened the coherent structures present at the same downstream location; and

3. The location of the step has a large effect. The further Further upstream the step location, the higher the coefficient of drag at high angles of attack.

4. The CVG outperforms a backward facing step, but not a clean wing, as shown by Fig. 40.

5.4.2. Phase II

1. The strong coherent structures produced by CVG-V1 that were discovered in phase I are repeatable. These structures not only persisted in the streamwise direction, but also in the vertical and spanwise directions.

2. There is a strong evidence that the CVG induces rotation in the flow. The vortices appear to co-rotate and there is a possibility that they are rotating about each other.

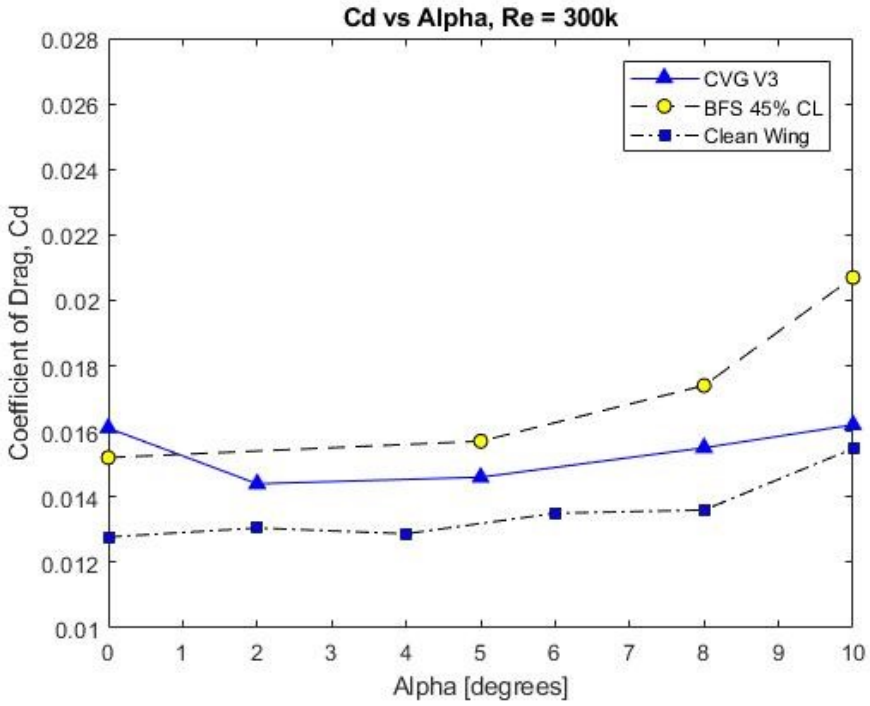

Figure 40: C_D plot comparing the best CVG, best BFS, and the clean wing results.

As expected, the CVGs do not actually outperform a clean wing. However, in practice, a perfectly clean wing is rare. For example, the Boeing 737 wing discussed earlier has a slat step at approximately 10 percent chord length that acts like a backward facing step. Mitigating the effects of the backward facing step through CVGs could lead to improved performance across certain flight regimes. For example, a leading mechanism for drag reduction could be through the strong coherent structures produced by the CVGs. These coherent structures could also explain the shock stabilization seen by Kibble [15]. To answer these questions, further testing is still required. However, what can be concluded is that the CVGs outperforming a backward facing step means that they have potential to be used in fields other than aircraft wings. As mentioned before, protective tapes have been used to protect the leading edge of helicopter blades and wind turbines. While not extensively studied, microsteps have been observed to have possibly significant impacts on boundary layer flows much larger than their step height would indicate [27–29]. In regions like this, CVGs could potentially reduce the increase in drag caused by the protective tapes

or joint geometries created by high lift devices.

CHAPTER VI

CONCLUSIONS AND RECOMMENDATIONS

6.1. Boundary Layer Investigation

An experiment investigating the boundary layer of a flat plate with CVG was conducted at the low speed water tunnel facility at Oklahoma State University. The flat was 750 mm long and 300 mm wide. A CVG tape was scaled and installed to the leading edge of the flat plate. The CVGs were 105 mm long and 76 mm wide. The thickness of the tape was 1.48 mm. Particle image velocimetry (PIV) was conducted at multiple locations downstream of the peak and the valley of the CVG. The velocity profiles at different locations were extracted and the boundary layer characteristics were investigated.A number of preliminary conclusions can be drawn from this study. Three primary determinations can be made about the flow physics are:

1. The flat plate was validated as the boundary layer profile followed the Blasius laminar solution at up to 370 mm downstream from the leading edge of the plate.

2. Boundary layer investigation shows that there is clear span wise variation in the velocity distribution. The variation can be seen up to 2 CVG lengths downstream of the peak.

3. The flow downstream of the peak transitions to a turbulent flow earlier than the

downstream of the valley. This occurs despite the step of the valley being much further than the step of the peak.

6.2. Wake Survey

A wake survey study was conducted at the subsonic wind tunnel at Oklahoma State University. A wing model with an LA203A profile was used for this study. The model had a chord length of 7.75 in and was 36 in wide. Clean wing, three backwards facing steps, and 4 CVG configurations were tested for this study. The thickness of the tape was 1.1 mm. For the first phase of the study, a single hole pitot-static probe was use to measure the stream wise velocity of the flow in the downstream wake region of the wing. From this study, velocity profiles were extracted and the coefficient of drag was calculated for all configurations. For the second phase of the study, A 5-hole probe was used to capture all three velocity components of the flow. The following conclusions can be drawn from the study:

6.2.1. Phase I

1. The CVG generates strong coherent turbulent structures that persist into the far wake region even at five chord lengths downstream of the wing;

2. Making the CVG sizes smaller weakened the coherent structures present at the same downstream location; and

3. The location of the step has a large effect. The further Further upstream the step location, the higher the coefficient of drag at high angles of attack.

4. The CVG outperforms a backward facing step, but not a clean wing, as shown by Fig. 40.

6.2.2. Phase II

1. The strong coherent structures produced by CVG-V1 that were discovered in phase I are repeatable. These structures not only persisted in the streamwise direction, but also in the vertical and spanwise directions.

2. There is a strong evidence that the CVG induces rotation in the flow. The vortices appear to co-rotate and there is a possibility that they are rotating about each other.

6.3. Recommendations

Although a few conclusions have been made on the efficacy of CVGs, further work is still necessary. Moving forward, the impact of the following may be evaluated:

1. A more in-depth spanwise PIV for the flat plate boundary layer investigation.

2. Study the impact of different CVG on the flat plate.

3. Conduct the wake survey experiment in the water tunnel for higher resolution data collection.

4. Conduct the wake survey in a supersonic wind tunnel to match the Boeing 737 flight conditions.

5. Different CVG Configurations: Only four CVG configurations were tested up to this point. The desire is to test many more by changing the dimensions and perhaps even the cross-sectional shape of the CVG.

REFERENCES

[1] Lin, J. C., "Review of research on low-profile vortex generators to control boundary-layer separation," *Progress in Aerospace Sciences*, Vol. 38, No. 4-5, 2002, pp. 389–420.

[2] Lin, J., "Control of turbulent boundary-layer separation using micro-vortex generators," *30th Fluid Dynamics Conference*, 1999, p. 3404.

[3] Shmilovich, A., and Yadlin, Y., "Flow control techniques for transport aircraft," *AIAA journal*, Vol. 49, No. 3, 2011, pp. 489–502.

[4] Yousefi, K., and Saleh, R., "Three-dimensional suction flow control and suction jet length optimization of NACA 0012 wing," *Meccanica*, Vol. 50, No. 6, 2015, pp. 1481–1494.

[5] López Calle, O., "Preliminary study of the effects of vortex generators in ultralight aircraft," B.S. thesis, Universitat Politècnica de Catalunya, 2015.

[6] McCormick, D., "Shock-boundary layer interaction control with low-profile vortex generators and passive cavity," *30th Aerospace Sciences Meeting and Exhibit*, 1992, p. 64.

[7] Dubey, A., Chheniya, S., and Jadhav, A., "Effect of Vortex generators on Aerodynamics of a Car: CFD Analysis," *International Journal of Innovations in Engineering and Technology (IJIET)*, Vol. 2, No. 1, 2013.

[8] Aider, J.-L., Beaudoin, J.-F., and Wesfreid, J. E., "Drag and lift reduction of a 3D bluff-body using active vortex generators," *Experiments in Fluids*, Vol. 48, No. 5, 2009, pp. 771–789. doi:10.1007/s00348-009-0770-y.

[9] Valdivia, A., Yuceil, K. B., Wagner, J. L., Clemens, N. T., and Dolling, D. S., "Control of Supersonic Inlet-Isolator Unstart Using Active and Passive Vortex Generators," *AIAA Journal*, Vol. 52, No. 6, 2014, pp. 1207–1218. doi:10.2514/1.j052214.

[10] Jacob, J., Rivir, R., Carter, C., and Estevadeordal, J., "Boundary Layer Flow Control Using AC Discharge Plasma Actuators," *2nd AIAA Flow Control Conference*, American Institute of Aeronautics and Astronautics, 2004. doi:10.2514/6.2004-2128.

[11] Santhanakrishnan, A., and Jacob, J. D., "Flow control with plasma synthetic jet actuators," *Journal of Physics D: Applied Physics*, Vol. 40, No. 3, 2007, pp. 637–651. doi:10.1088/0022-3727/40/3/s02.

[12] "Conformal Vortex Generators," , 2017. URL `https://edgeaerodynamix.wordpress.com`.

[13] Calvert, M., and Wong, T.-C., "Aerodynamic Impacts of Helicopter Blade Erosion Coatings," *30th AIAA Applied Aerodynamics Conference*, 2012, p. 2914.

[14] Scholbrock, A., "Power Performance Results Using Wind Turbine Blade Enhancing Devices Developed By Edge Aerodynamix," Tech. rep., National Renewable Energy Laboratory, 2017.

[15] Kibble, G. A., "Experimental and Computational Investigation of the Conformal Vortex Generator," Master's thesis, Oklahoma State University, 2017.

[16] Lucido, N., KC, R., Wilson, T., Jacob, J., Alexander, A., Elbing, B., Ireland, P., and Black, J., "Laminar Boundary Layer Scaling Over a Conformal Vortex Generator," *2019 AIAA Aerospace Sciences Meeting*, 2019.

[17] Wilson, T., KC, R., Lucido, N., Jacob, J., Alexander, A., Elbing, B., Ireland, P., and Black, J., "Computational Investigation of the Conformal Vortex Generator," *2019 AIAA Aerospace Sciences Meeting*, 2019.

[18] KC, R., Lucido, N. A., Wilson, T. C., Elbing, B. R., Jacob, J. D., Alexander, A. S., Ireland, P., and Black, J. A., "Investigation of Wake Survey over a Wing with Conformal Vortex Generators," *AIAA Scitech 2019 Forum*, 2019, p. 0578.

[19] Kundu, P. K., *Fluid mechanics*, sixth edition.. ed., Academic Press, 2016.

[20] Lucido, N. A., "Investigation of Low-Profile Vortex Generators on Low Reynolds Number Propellers for Small Unmanned Aircraft," Master's thesis, Oklahoma State University, 2019.

[21] Drela, M., "XFOIL Subsonic Airfoil Development System," , 2018. URL `http://web.mit.edu/drela/Public/web/xfoil/`.

[22] Schlichting, H., and Gersten, K., *Boundary-layer theory*, ninth ed., Springer, 2016.

[23] Patel, V., "Calibration of the Preston tube and limitations on its use in pressure gradients," *Journal of Fluid Mechanics*, Vol. 23, No. 1, 1965, pp. 185–208.

[24] Tropea, C., and Yarin, A. L., *Springer handbook of experimental fluid mechanics*, Vol. 1, Springer Science & Business Media, 2007.

[25] Zimbelman, T., "Plasma Flow Control for Distortion Tolerant Fans with Aircraft Boundary Layer Ingestion," Master's thesis, Oklahoma State University, 2018.

[26] Brune, G. W., "Quantitative Low-Speed Wake Surveys," *AIAA Journal of Aircraft*, Vol. 31, No. 2, 1994, pp. 249–255.

[27] Falco, R., "Drag Reduction Method and Surface," *US Patent 5,133,519*, 1992.

[28] Hollon, B., and Jacob, J., "Flow Visualization by Particle Deposition of Reattachment Behind a Backward Facing Microstep," *54th Annual Meeting of the Division of Fluid Dynamic Gallery of Fluid Dynamics*, 2001.

[29] Al-Jaburi, K., and Feszty, D., "Passive Flow Control of Dynamic Stall via Surface-Based Trapped Vortex Generators," *Journal of the American Helicopter Society*, Vol. 63, No. 3, 2018, pp. 1–14.

APPENDICES

An attempt was made to conduct Particle Image velocimetry (PIV) on the airfoil model with CVG-V2 in the wind tunnel. Due to the unstable fog and seeding difficulty inside the wind tunnel, PIV was deemed impossible with the current setup. However, some high speed images were taken to capture the flow downstream of the peak, mid, and the valley, as shown in Fig. 41. The flow downstream of the peak (top) seemed to be turbulent soon after the flow went over the peak. The mid location seemed to be transitioning as the boundary layer was shorter than that of the peak. For valley, there seemed to be no sign of turbulence at all, as the flow seemed to go smoothly over the wing past the valley. This is another evidence of the earlier statement that the peak transitions earlier than the valley even though the valley is located further downstream on the wing than the valley.

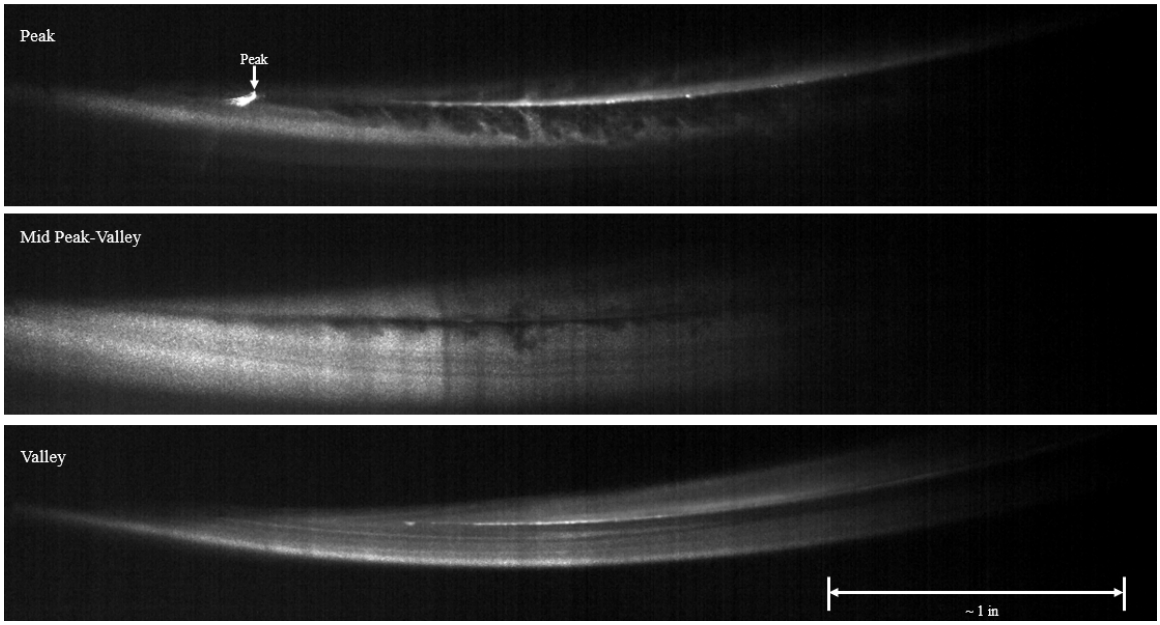

Figure 41: Flow visualization of the flow downstream of CVG-V2 (top) peak, (middle) mid peak-valley, and (bottom) valley.

VITA

Real KC

Candidate for the Degree of

Master of Science

Thesis: INVESTIGATION OF LOW-PROFILE VORTEX GENERATORS VIA EXPERIMENTAL METHODS

Major Field: Mechanical and Aerospace Engineering

Biographical:

Education:

Completed the requirements for the Master of Science in Mechanical and Aerospace Engineering at Oklahoma State University, Stillwater, Oklahoma in July, 2019.

Completed the requirements for the Bachelor of Science in Aerospace Engineering at Oklahoma State University, Stillwater, Oklahoma in May, 2017.